Modeling and Simulation of Vibration Isolation System for Large-scale Cryogenic Gravitational-wave Telescope (LCGT)

Department of Physics
School of Science
University of Tokyo

Takanori Sekiguchi

Jan. 2012

Contents

Chapter 1

Detection of Gravitational Waves

1.1 Gravitational Waves

Gravitational waves, which are predicted by Einstein's theory of general relativity in 1916, are often described as "ripples in space-time". Within the weak-field approximation of Einstein's equation, a wave equation is derived as [1]

$$\left(\nabla^2 - \frac{1}{c}\frac{\partial^2}{\partial t^2}\right) h_{\mu\nu} = 0, \tag{1.1}$$

where $h_{\mu\nu}$ represents a deviation of space-time metric from Minkowskii metric:

$$g_{\mu\nu} = \eta_{\mu\nu} + h_{\mu\nu} \quad (|h_{\mu\nu}| \ll 1). \tag{1.2}$$

This equation indicates that small distortions of space-time $h_{\mu\nu}$ propagate at the speed of light. These distortions are called *gravitational waves*.

Within the transverse-traceless (TT) gauge, gravitational waves propagating in z-direction are represented by a linear combination of two polarizations:

$$h_+ = A_+ \begin{pmatrix} 0 & 0 & 0 & 0 \\ 0 & 1 & 0 & 0 \\ 0 & 0 & -1 & 0 \\ 0 & 0 & 0 & 0 \end{pmatrix}, \; h_\times = A_\times \begin{pmatrix} 0 & 0 & 0 & 0 \\ 0 & 0 & 1 & 0 \\ 0 & 1 & 0 & 0 \\ 0 & 0 & 0 & 0 \end{pmatrix}. \tag{1.3}$$

h_+ and $h_\times$ are called *plus* and *cross mode* of gravitational waves, respectively.

Gravitational waves exert tidal forces onto free particles. Consider an array of particles circularly arranged in xy-plane. The tidal effect of a passing gravitational wave, propagating in the z-axis, is visualized in Figure 1.1. The tidal effect stretches space-time in one direction while compressing it by an equal amount in the perpendicular direction. The two polarizations of the gravitational wave, h_+ and $h_\times$ are identical and 45° apart.

Gravitational waves are emitted when mass is accelerated. Since conservation of mass and linear momentum forbid monopole and dipole radiation of gravitational waves, the lowest order emission is quadrupole. Using the quadrupole approximation, the amplitude of the gravitational wave is calculated as [1]

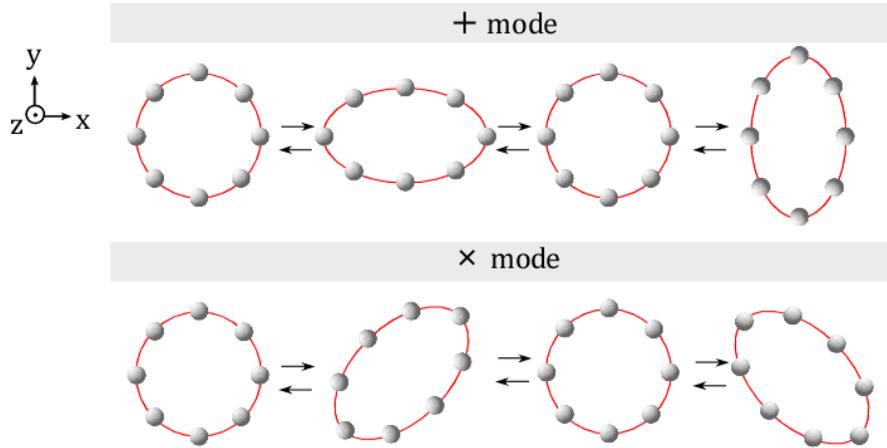$$h_{ij} = \frac{2G}{c^4 R}\ddot{Q}_{ij}, \tag{1.4}$$

Figure 1.1: Tidal effect of gravitational waves

where Q_{ij} is the quadrupole moment of the mass distribution, G is the gravitational constant and R is the distance between the source of gravitational waves and the observer. The amplitude of the gravitational wave expected from the formula (1.4) is extremely small. For example, two 100 kg masses connected with 2 m beam, rotating 100 cycles per second will emit 200 Hz gravitational wave of amplitude only $h \sim 10^{-43}$ at a distance of 1500 km [2]. It is impossible to detect such a tiny distortion of space-time.

Detectable gravitational waves only come from violent astronomical events, which involve large acceleration of very compact massive objects moving at about the speed of light, to offset the c^{-4} term. Typical sources of gravitational waves are coalescence of compact star binaries [3], stellar-core collapse in supernovae [4], rotating neutron stars [5] and background radiation from the early universe [6].

1.2   Interferometric Detection of Gravitational Waves

The first attempt to detect gravitational waves was performed in 1960's by J. Weber [7]. He invented the resonant-bar detectors, which were designed to detect the resonant vibrations of massive metal bars excited by passing gravitational waves. However, the resonant-bar detectors did not reach sufficient sensitivity to detect gravitational waves and allowed for only narrow-band observation.

Nowadays, gravitational wave detectors are mainly based on interferometric techniques. The basic configuration of the interferometric gravitational wave detector is a Michelson interferometer which consists of suspended masses. Its optical configuration is shown in Figure 1.2. An incoming beam from a coherent light source is split by the beam splitter into two orthogonal paths. The two beams are reflected by the end mirrors and recombined at the beam splitter. They interfer with each other, and a fraction of beam goes to the photo detector and the rest goes back to the light source. The intensity at the photo detector depends on the phase difference accumulated in the two optical paths.

Suppose that a gravitational wave comes from z-direction with h_+ polarization and amplitude of $h(t)$. The phase difference of the two optical paths caused by the gravitational
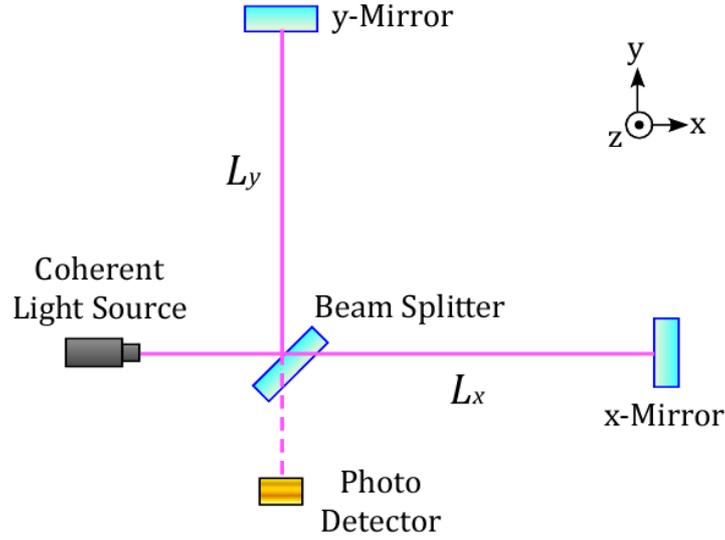
Figure 1.2: A Michelson interfoerometer.

wave is calculated as [8]

$$\delta\phi_{\mathrm{GW}}(t) = \frac{2\pi c}{\lambda} \int_{t-2L/c}^{t} h(t')dt',$$ (1.5)

where λ is the wavelength of the laser beam and L is the length of the arms ($L_x \approx L_y \approx L$). The frequency response of the Michelson interferometer to gravitational waves is derived from the Fourier transform of this equation as

$$H_{\mathrm{MI}}(\omega) \equiv \frac{\tilde{\phi}_{\mathrm{GW}}(\omega)}{\tilde{h}(\omega)} = \frac{4\pi L}{\lambda} \exp(-i\omega L/c)\frac{\sin(\omega L/c)}{\omega L/c}.$$ (1.6)

Figure 1.3 shows the plots of $|H_{\mathrm{MI}}|$ as a function of frequency with various arm lengths. When the arm length is much shorter than the wavelength of the gravitational wave ($L \ll \lambda_{\mathrm{GW}}$), the frequency response is approximated as $H_{\mathrm{MI}} \sim 4\pi L/\lambda$. It indicates that a detector with longer arms is more sensitive to gravitational waves. However, when the arm length gets longer than the wavelength of the gravitational wave ($L \gtrsim \lambda_{\mathrm{GW}}$), canceling of the gravitational wave signals occurs. $|H_{\mathrm{MI}}|$ is maximized at

$$L = \frac{\pi c}{2\omega} = \frac{\lambda_{\mathrm{GW}}}{4}.$$ (1.7)

For a gravitational wave of 100 Hz, the optimum arm length is about 750 km. It is unrealistic to construct such a large interferometer on the Earth.

In order to extend the optical path length and to optimize the frequency response, the optical paths are enhanced by using delay-lines or Fabry-Perot cavities. The Michelson interferometer with folded arms is called delay-line-Michelson interferometer (Figure 1.4). If a Fabry-Perot cavity is used, the detector is called a Fabry-Perot-Michelson interferometer (Figure 1.5).
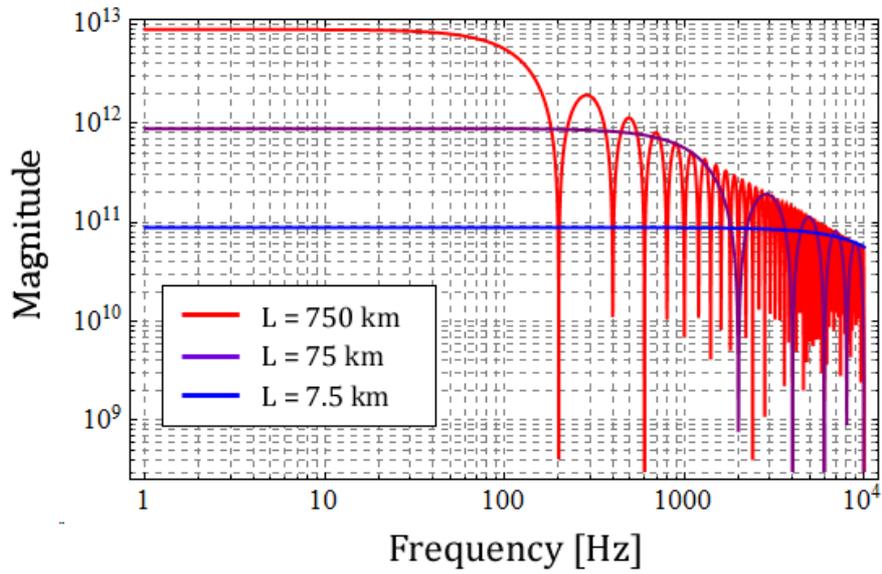
Figure 1.3: Frequency response of the Michelson interfoerometer with various arm lengths
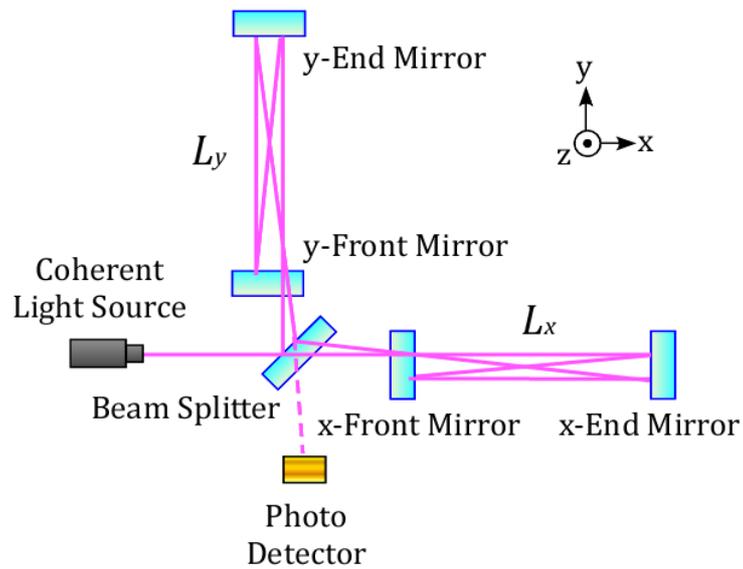

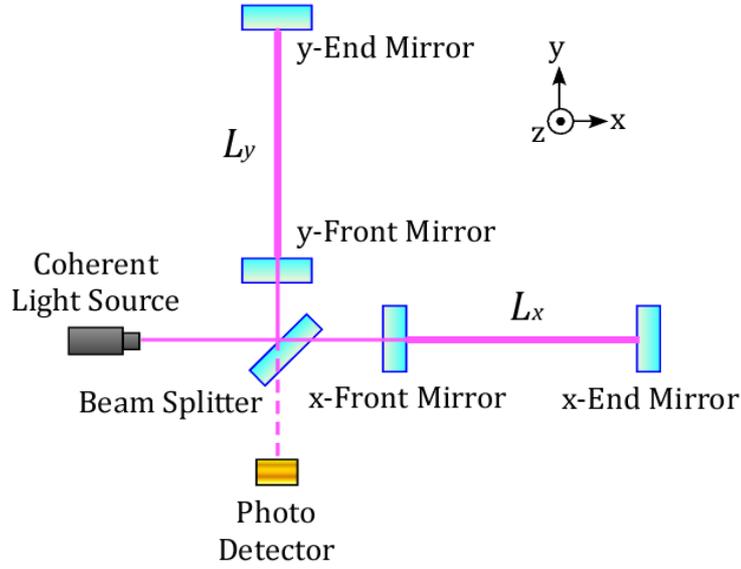Figure 1.4: A delay-line-Michelson interferometer of 4 reflection.

Figure 1.5: A Fabry-Perot-Michelson interferometer.

A delay-line is composed of two mirrors. One of them has a small hole to inject the laser beam in it. The incoming beam is multiply reflected at the different points on the surface of the mirrors forming a Lissajou pattern, then ejected back through the same hole. When the beam is reflected $(N-1)$ times in the delay-line, the total optical length is calculated as NL, where L is the distance between the two mirrors. The expression for the frequency response of a delay-line-Michelson interferometer to gravitational waves $H_{\mathrm{DLMI}}(\omega)$ is obtained by replacing $2L$ of $H_{\mathrm{MI}}(\omega)$ in (1.6) by NL:

$$H_{\mathrm{DLMI}}(\omega) = \frac{2\pi NL}{\lambda} \exp(-i\omega NL/2c) \frac{\sin(\omega NL/2c)}{\omega NL/2c}. \tag{1.8}$$

The folded path suffers from severe thermal noise limitations, and is practically unused in gravitational wave detectors today.

The optical path length can be also exteded by the multiple interference of a Fabry-Perot cavity. A Fabry-Perot cavity is composed of two mirrors and one of them is partially reflective. The light entered into the cavity is reflected back and forth many times between the mirrors. A fraction of the stored light inside the cavity is leaked out and goes back to the incident direction. The frequency response of a Fabry-Perot-Michelson interferometer to gravitational waves $H_{\mathrm{FPMI}}(\omega)$ is written as

$$H_{\mathrm{FPMI}}(\omega) = \frac{4\pi\alpha_{\mathrm{cav}}L}{\lambda} \frac{\exp(-i\omega L/c)}{1 - r_{\mathrm{F}}r_{\mathrm{E}}\exp(-2i\omega L/c)} \frac{\sin(\omega L/c)}{\omega L/c}, \tag{1.9}$$

when two Fabry-Perot cavities are in resonance [8]. α_{cav} is calculated as

$$\alpha_{\mathrm{cav}} = \frac{t_{\mathrm{F}}^2 r_{\mathrm{E}}}{1 - r_{\mathrm{F}}r_{\mathrm{E}}}, \tag{1.10}$$

where r_{F} and $r_{\mathrm{E}} \sim 1$ are the amplitude reflectivity of the front and end mirrors, and t_{F} is the transsissivity of the front mirror. L is the length of the Fabry-Perot cavity. The

average bounce number in a Fabry-Perot cavity is written as

$$N_{\mathrm{FP}} = \frac{2\sqrt{r_{\mathrm{F}}r_{\mathrm{E}}}}{1 - r_{\mathrm{F}}r_{\mathrm{E}}} = \frac{2\mathcal{F}}{\pi}. \tag{1.11}$$

$\mathcal{F}$ is called a finesse, which represents the sharpness of the resonance of the Fabry-Perot cavity.

Figure 1.6 shows the plots of $|H_{\mathrm{DLMI}}|$ and $|H_{\mathrm{FPMI}}|$ as a function of frequency. In both cases, the arm length is 3 km and the response is optimized for a gravitational wave with a frequency of 100 Hz. For comparison, the frequency response of a Michelson interferometer with the same arm length is drawn in Figure 1.6. The curve of response of the Fabry-Perot-Michelson interferometer is smoother than that of the delay-line-Michelson interferometer.
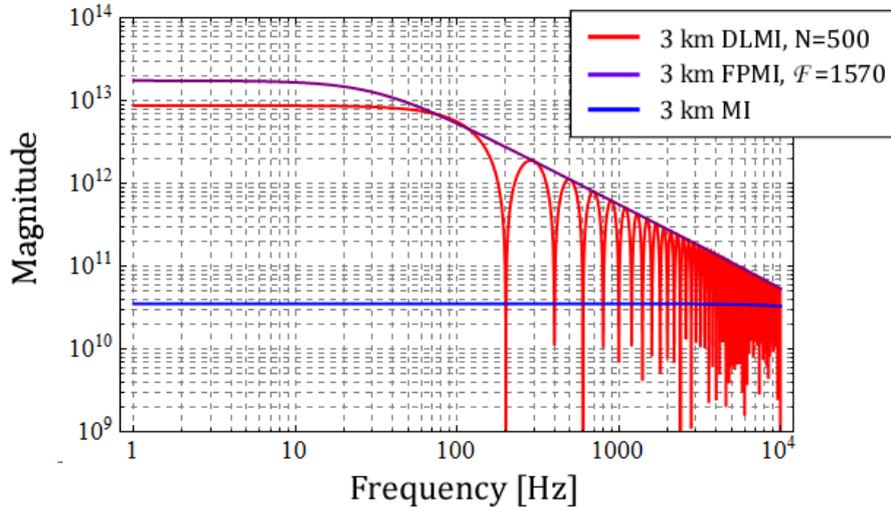

Figure 1.6: The frequency response of the delay-line-Michelson, Fabry-Perot-Michelson and simple Michelson interferometer. The arm lengths are 3 km in all cases. The frequency response of delay-line-Michelson and Fabry-Perot-Michelson interferometer is optimized for a gravitational wave of 100 Hz.

1.3 Noise Sources

The sensitivity of an interferometeric gravitational wave detector can be easily degraded by various noise sources, which are briefly explained here.

Seismic Noise

The sensitivity of a ground-based interfermeter is ultimately limited by the seismic motion at low frequencies. Unless properly isolated from, the vibration of the ground can excite the motions of optical components of an interferometer, resulting in a displacement noise. This is called the *seismic noise.*

In order to reduce the seismic noise, vibration isolation systems are installed to isolate the optics in the interferometer. General discussions on the seismic motion and vibration isolation systems are given in section 1.2.

Although the direct mechanical influence of the seismic noise can be isolated ideally at will by the use of a suitable number of attenuating stages, the direct coupling of seismic noise to the test masses through Newtonian gravitational attraction can not be shielded. This noise, called the *Newtonian noise*, is the eventual limit of gravitational wave detection on Earth. It can be reduced by moving the interferometer underground, where the rock in the vicinity of the test mass is more rigid and moves less under the effects of the seismic noise field. The Newtonian noise can also be calculated and subtracted if the seismic noise of the rock is detected by an array of seismometers.

Thermal Noise

The mirrors and their suspension systems are in the thermal bath and recieve the energy at random. This random energy flow causes the fluctuations of the surface and center of the mirrors, in short, the arm length of the interferometer. This noise is called the *thermal noise.*

The amount of the thermal fluctuation is related to the loss of the system by fluctuation-disspiation theorem [9]. In order to reduce the thermal noise, one needs to use high quality materal for the mirrors and their suspensions. Since fused silica has a high quality factor ($\sim 10^7$) at room temperature [10] and good optical property, it is used for the mirror substrates in many interferometric gravitational wave detectors, and also for their suspension fibers in some advanced detectors.

The thermal noise can be also reduced by lowering the temperature. Since fused silica has low quality factor at low temperature, it becomes unusable in cryogenic systems. On the other hand, sapphire and silicon have high quality factors ($\sim 10^8$) and large thermal conductivity at cryogenic temperature [11, 12], and are good candidates for the mirror substrates for cryogenic detectors.

Shot Noise

The shot noise is a fundamental disturbance of optical length sensing associated with the quantum nature of light. The interferometer light output is proportional to the longitudinal movement of the mirrors. A photo detector counts the number of photons in a certain measurement time and produces photo currents proportional to the incident power. In

this process, the counted number of photons (i.e. electrons produced and contributing to the current) has the Poisson distribution, which results in fluctuation of photon number. The noise induced by this fluctuation is called the *shot noise.*

The fluctuation of length sensing due to the probability distribution is proportional to the square-root of the incident power on the mirrors $\sqrt{P_{\text{in}}}$. On the other hand, the signal amplitude of the gravitational wave is proportional to P_{in}, therefore the signal to noise ratio is proportional to $1/\sqrt{P_{\text{in}}}$.

Consequently, the shot noise can be reduced by increasing the power of the laser. This is why laser with high power (close to 200 W) is necessary for advanced detectors. In order to increase the effective power on the mirrors, high finesse Fabry Perot cavities are implemented in the interferometer cavities, and in addition, a technique called "power recycling" [13] is used as well. In this technique, a partial reflective mirror is placed between the laser and the beam splitter (Figure 1.7) with the appropriate phase, to reflect the light returning from the beam splitter and send it back to the Michelson interferometer.
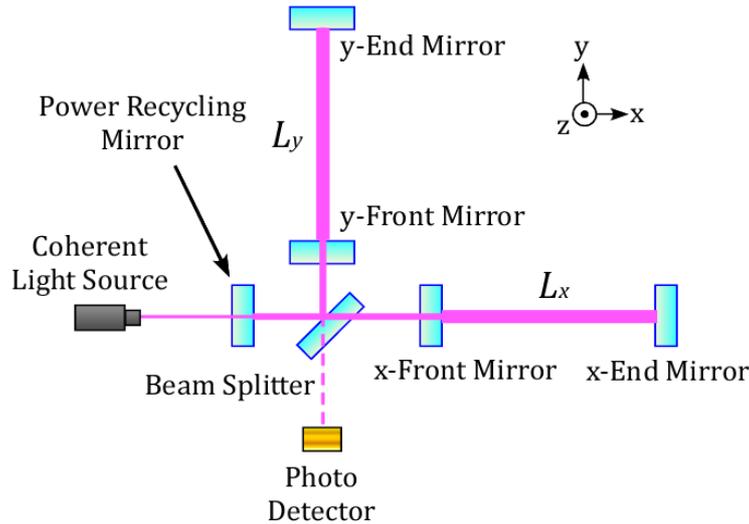
Figure 1.7: A Fabry-Perot-Michelson interferometer with power recycling.

Radiation Pressure Noise

When a photon is reflected by a mirror, a back action force is exerted onto it. Owing to the quantum nature of light, the number of the photons hitting on the mirror fluctuates and therefore the back action force fluctuates. The displacement noise caused by this fluctuation is called the *radiation pressure noise.*

The fluctuation force is proportional to the square-root of the laser power $\sqrt{P_{\text{in}}}$. Since the shot noise is proportional to $1/\sqrt{P_{\text{in}}}$, there is a trade-off between the shot noise and the radiation pressure noise. Owing to this characteristic, there is a limit on the sensitivity of an interferometer called the standard quantum limit (SQL). This corresponds to the quantum mechanical limit of the masurement from the Heisenberg uncertainty principle. Currently various methods to beat this limit are proposed [14].

Laser Noise

As a laser interferometric gravitational wave detector measures the length between the mirrors using the wavelength of the laser as a reference, the noises in the laser contaminates its sensitivity.

The frequency fluctuation of the laser is in principle cancelled at the interference, if the two arms of the interferometer are identical. However, it is not completely cancelled in a real system because of a small asymmetry of the two arms. Therefore the frequency of the laser is stabilized by feedback controls. One of the two Fabry-Perot cavities is used as a reference cavity for the feedback for the laser frequency stabilization.

The intensity fluctuation also introduces a noise to the output signal of the interferometer. The effect of the intensity fluctuation is minimized when the interferometer is operated at a dark fringe. However, in practice, there remains a light intensity by the residual motion of the mirrors. The fluctuation of this intensity contaminates the output of the detector; intensity noise. and the residual motion around the fringe couples with the intensity noise of the laser. Therefore the intensity of the laser has to be stabilized and the control gain has to be large enough to suppress the residual motion of the mirror.

Residual Gas Noise

The random motions of molecules in the vacuum pipes cause fluctuation of the index of refraction in the optical paths of an interferometer. This causes the fluctuation of the effective arm lengths. In order to reduce the effect of residual gas fluctuation, interferometers are operated in an ultrahigh vacuum (10^{-6}-10^{-7} Pa).

Control System Noise

During the operation of an interferometer, the optical components of the interferometer are controlled to keep the Fabry-Perot arms and power recycling cavity in resonance and the detection port at a dark fringe. Several auxiliary beam monitoring signals are used for these feedback loops. Detection and digitization noise of these auxiliary detectors, as well as the noise of the electric circuits for the control may contaminate the sensitivity of the interferometer. Although this is not a fundamental noise, careful consideration and design are required to minimize this noise.

1.4 Detector Projects

Ground-based, large scale interferometric gravitational wave detectors operated or planned are summerized in Table 1.1 [15].

The first generation detectors (TAMA [16], GEO [17], LIGO [18], Virgo [19]) have performed scientific observations since 1999. The first generation detector had a detection probability of a few percent per year. Although gravitational waves have not been detected by these detectors, they demonstrated the effectiveness of the working principle and set some upper limits to the gravitational wave sources.

Based on the experience gathered with the first generation detectors, second generation ones have been designed, with thousands of times higher probability of gravitational wave

Generation	Project	Country	Baseline Length	Observation
1st	TAMA	Japan	300 m	1999∼
	GEO	Germany, U.K.	600 m	2000∼
	LIGO	U.S.A.	4 km	2001∼
	VIRGO	Italy, France	3 km	2002∼
2nd	Adv. LIGO	U.S.A.	4 km	2016∼
	Adv. Virgo	Italy, France	3 km	2016∼
	LCGT	Japan	3 km	2017∼
3rd	ET	Europe	10 km	2025∼

Table 1.1: Ground-based interferometric gravitational wave detector projects.

detection. Several first generation detectors were upgraded (enhanced LIGO, Virgo+), with the sensitivities improved by introducing higher power lasers and advanced techniques such as monolithic suspensions [19]. They are going to be upgraded to the second generation detectors (advanced LIGO, advanced Virgo) and are scheduled to start observation in 2016.

A Japanese second generation detector, LCGT (Large-scale Cryogenic Gravitational wave Telescope) [20], was funded recently and is now being constructed. In addition to the same improvements of the advanced interferometers, it features the use of cryogenic mirrors and underground environment, which are unique characteristics in the first and second generation detectors. The observation of LCGT is scheduled to start in 2017.

To go beyond the sensitivities of these detectors, there is a plan to construct a third generation detector, ET (Einstein Telescope) [21], which has been designed by European research institutes. It aims to reach a sensitivity about a factor of 10 better than the second generation detectors. Also space-borne detectors (LISA [22], DECIGO [23]) have been studied, aiming for the observation of low frequency gravitational waves.

1.5   LCGT

LCGT has been designed to detect several gravitational wave events per year, optimized for the coalescences of neutron star binaries. The LCGT nominal design is to detect the coalescence signal of double neutron stars ($1.4M_\odot + 1.4M_\odot$) at a distance of ∼250 Mpc with SNR = 10, assuming sources are at the optimal orientation with respect to the detector at the time of the event [20].

The detector will be constructed underground in the Kamioka mine, Gifu prefecture, to get the benefit of quiet seismic activities and stable environment (Figure 1.8).

The detector adopts a power-recycled Fabry-Perot-Michleson interferometer with Resonant Sindeband Extraction (RSE) scheme, and has 3 km arm length. Its optical design is shown in Figure 1.9. The optical parameters such as the power recycling gain, the signal bandwidth and the arm finesse are optimized to maximize the event rate for inspirals of neutron star binaries.

The test masses will be 23 kg cylinders made of sapphire substrates with reflective dielectric coatings, and will be cooled at about 20 K to reduce the thermal noise. They will be suspended by sapphire fibres with moderate thickness, to transfer the heat absorbed

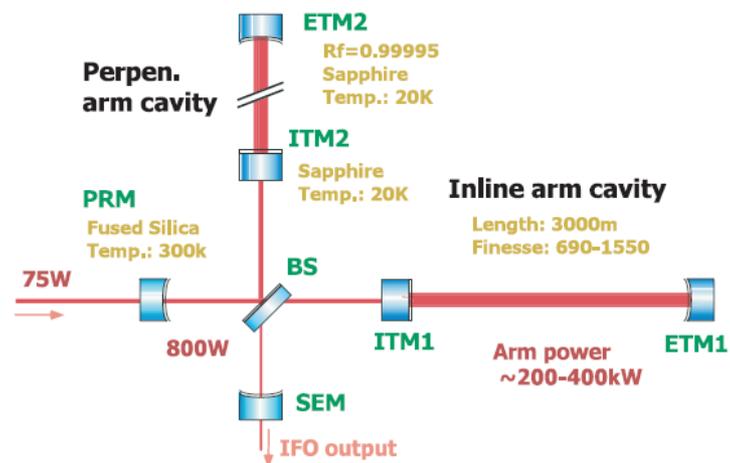Figure 1.8: An impression of LCGT in the Kamioka mine.

Figure 1.9: The optical design of LCGT.

in the mirror from the high power laser beams. Since commercial cryocoolers generally cause large vibration and polute the quiet environment of the underground site, specially designed pulse-tube cryocoolers [24] are used and passive isolation techniques will be used to isolate the vibrations generated by the cryocoolers.

The optical paths will be kept in 2×10^{-7} Pa of vacuum pressure to reduce optical length fluctuations due to residual gas molecules [25]. The seismic noise is reduced by employing sophisticated anti-vibration system, SAS (Seismic Attenuation System), for the optical components forming the interferometer.

The expected sensitivity of the planned detector is shown in Figure 1.10. Since the thermal noise is suppressed at cryogenic temperature, the sensitivity is mainly limited by the optical quantum noise at the frequencies higher than 10 Hz. At low frequencies, the sensitivity is limited by the seismic noise.
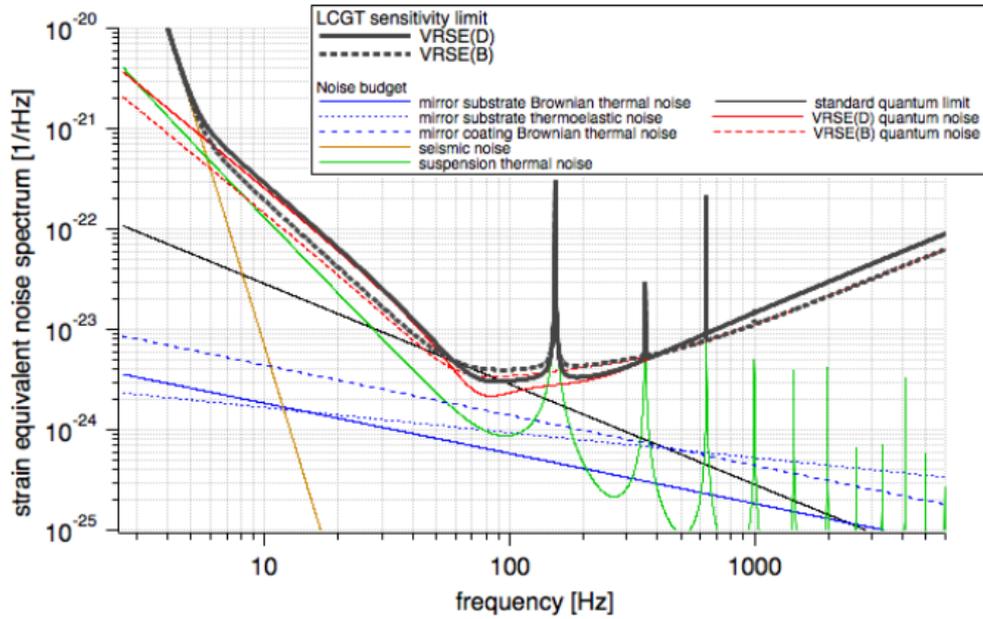

Figure 1.10: The expected sensitivity of LCGT [26].

Chapter 2

Seismic Isolation

2.1 Seismic Spectrum

Seismic motion is an inevitable noise source for ground-based interferometic gravitational wave detectors. The continuous and random motion of the ground is induced by natural phenomena like oceanic and astropheric activities, as well as by human activities. The amplitude of the seismic motion varies by few orders of magnitude from site to site and from time to time, depending on the surrounding environment such as weather and traffic condition in nearby cities. In most cases it has almost the same amplitude in all three orthogonal directions, and at high frequencies the spectrum density of the displacement is typically written in the form of

$$\tilde{x}_{\mathrm{seism}}(f) = A \times (f/1 \text{ Hz})^{-2} \text{ m}/\sqrt{\text{Hz}} \quad (f > 1 \text{ Hz}). \tag{2.1}$$

The constant A varies from 10^{-9} to 10^{-6} depending on the sites.
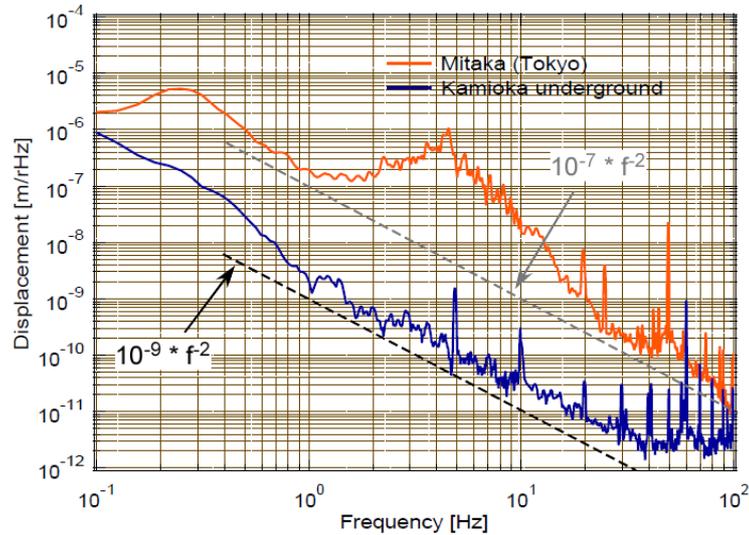

Figure 2.1: Spectrum density of seismic vibration in Mitaka (TAMA site) and Kamioka mine (LCGT site) [27]

Figure 2.1 shows the spectrum density of the ground motion displacement observed in Mitaka (TAMA site) and the Kamioka mine (LCGT site). The amplitude of the ground

motion in the Kamioka mine is smaller than that of Mitaka by 2-3 orders of magnitude. Generally, seismic activities are relatively quiet in underground environment [28], because atmospheric fluctuations are relatively far and human activities are limited. LCGT will be constructed underground to get the benefit of these characteristics.

The broad peak observed between 0.1 and 0.3 Hz in the spectrum of Mitaka is called the *microseismic peak*, which is induced by oceanic wave activities [29]. The peak is observed strongly along the coast and weakly in the middle of continents [30]. The noise due to human activities is mostly observed in the frequency range of 1-10 Hz [28].

Since the amplitude of the ground motion is around $10^{-12} \sim 10^{-10}$ m/$\sqrt{\text{Hz}}$ at 100 Hz, and the expected amplitude of the arm length variation due to a gravitational wave is typically in the order of 10^{-20} m/$\sqrt{\text{Hz}}$ at that frequency, an attenuation factor of $10^{-10} \sim 10^{-8}$ is required for the detection of gravitational waves.
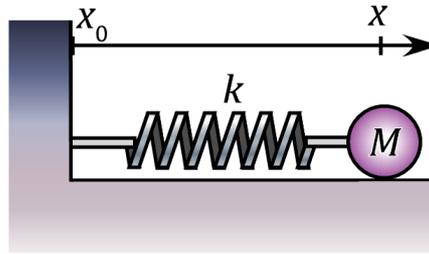
2.2   Passive Mechanical Filters

Figure 2.2: An example of the mechanical filter

Isolation from seismic motion can be realized by the use of mechanical filters with elastic components, such as springs and pendulums. As the simplest example, consider a one-dimensional spring-mass system shown in Figure 2.2. The equation of motion of this system is written as

$$M\ddot{x} = -k(x - x_0). \tag{2.2}$$

Here x and x_0 are the position of the bob and the suspension point. M is the mass of the bob and k represents the stiffness of the spring. This equation can be solved in the frequency domain by taking Fourier transform. Defining the angular resonant frequency of the pendulum as $\omega_0 = (k/M)^{1/2}$, one obtains the following equation:

$$H(\omega) \equiv \frac{\tilde{x}(\omega)}{\tilde{x}_0(\omega)} = \frac{1}{1 - (\omega/\omega_0)^2}. \tag{2.3}$$

$H(\omega)$ is called the *transfer function* from the motion of the suspension point to the bob motion. The amplitude of $H(\omega)$ is plotted as a function of frequency in Figure 2.3.

From this figure, one can see the general behavior of mechanical filters. In the low frequency region ($f \ll f_0$), the transfer function is close to one, which means that the motion of the bob follows that of the suspension point. Around the resonance, the amplitude of the transfer function increases and, in absence of dissipation, goes to infinity at
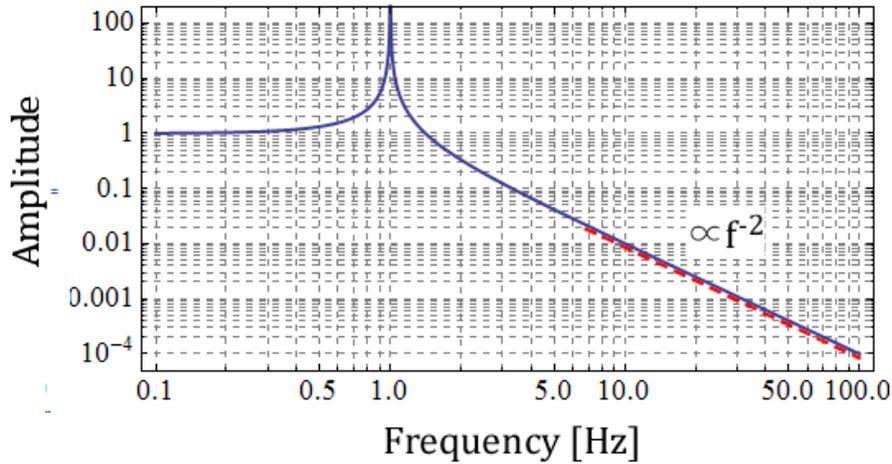
Figure 2.3: The amplitude of the transfer function of a mechanical filter whose resonant frequency is $f_0 = 1$ Hz.

the resonance. In a high frequency region ($f \gg f_0$), the amplitude of the transfer function rolls off in proportion to f^{-2}, so that the suspended mass is progressively isolated from the vibration of the support point in this frequency region. As the vibration isolation ratio is written as $(f/f_0)^{-2}$ at any given frequency above the resonace, the suspended mass is isolated more when one uses a mechanical filter with a lower resonant frequency.

In an interferometric gravitational wave detector, which is a horizontal instrument, every test mass is suspended as a pendulum so that it behaves as a free particle in the sensitive plane of the interferometer. This suspension also works as an isolator from the ground vibration. The resonant frequency of the pendulum is around 1 Hz with a reasonable length (a few tens of cm), therefore the vibration isolation ratio is about 10^{-4} at 100 Hz. Since the required attenuation is around $10^{-10} \sim 10^{-8}$, seismic attenuation by a simple pendulum is not sufficient for the detection of gravitational waves.

The required seismic attenuation is obtained by cascading mechanical filters, whose resonant frequencies are sufficiently lower than the frequency region of interest ($\gtrsim 10$ Hz). In an N-stage chain of mechanical filters, the ground motion transmits to the suspended mass with an attenuation proportional to f^{-2N}, at a frequency higher than the resonant frequencies of the chain. Figure 2.4 shows the attenuation performance of a multi-stage pendulum with various stage numbers. Using a sufficient number of attenuation stages, a very large attenuation of the ground vibration can be obtained in the high frequency region.

2.3   Couplings from Vertical and Rotational Motion

Since the horizontal ground motion transmits directly to the horizontal motions of the mirrors and contributes to the changes in the optical path lengths of the interferometer, isolation from the horizontal ground vibration is the most critical issue in seismic isolation. However, isolation from the vertical ground vibration is also indispensable in practice. This is because 0.1-1% of the vertical motion is transferred to the horizontal direction at each
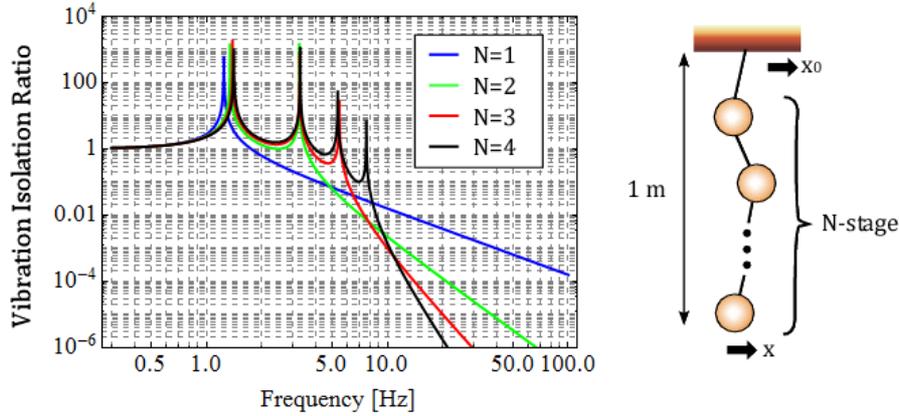
Figure 2.4: The amplitude of the transfer functions of N-stage pendulums with $N = 1 \sim 4$. The total length of the pendulum is $L = 1$ m in all cases.

attenuation stage by mechanical imperfections.

Ultimately, vertical noise is coupled to the longitudinal direction by the non-parallelism of the verticality at kilometers apart locations in the interferometer. As shown in Figure 2.5, the front and end mirrors of the Fabry-Perot cavities form an angle of $\alpha = L/2R_\oplus$ with the interferometer's global vertical direction. Here L is the cavity length and $R_\oplus$ is the radius of the Earth. Thence a vertical displacement δz has an effect along the beam direction, producing a variation $\alpha \delta z$ of the cavity length. In the case of 3-km length interferometer, the minimum coupling due to the Earth curvature is calculated as $\alpha \sim 2 \times 10^{-4}$.
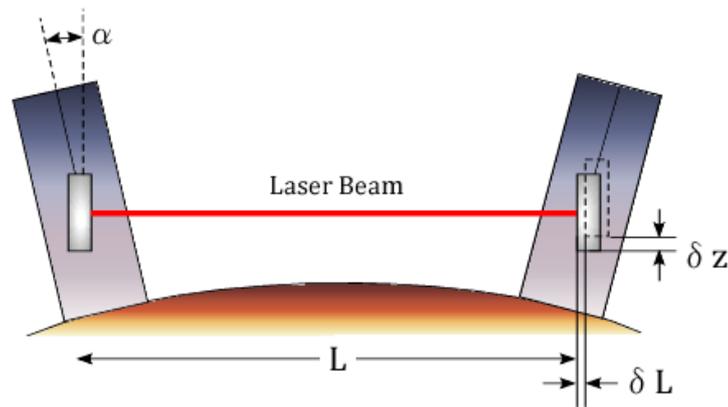
Figure 2.5: Effect of the Earth curvature.

Not only the vertical motions, but also the rotational motions of the mirror may affect the sensitivity of the interferometer. The rotational motion of a mirror does not change the optical path length ideally if the laser beam illuminates the center of the mirror. However, the beam spot is off-centered to some extent in reality, and an angular displacement causes a variation of the optical path length as shown in Figure 2.6.

Figure 2.6: Coupling from the rotational motion of the mirror due to misalignment.

2.4 Damping

Stable Operation of Interferometers

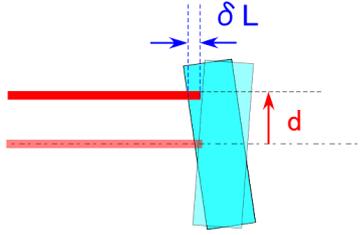Seismic motion affects not only the sensitivity of the interferometer, but also its stability. Although the chains of mechanical filters isolate the optics from seismic motion at a high frequency region, the mirror motions can be largely excited at low frequencies, especially at the resonant frequencies of the mechanical system. As the interferometer must be kept in the dark fringe condition by feedback controls, the RMS (Root Mean Square) amplitude of the mirror displacement have to be suppressed to within the limited dynamic range of the controls.

The RMS amplitude of the ground motion displacement (integrated up to $\lesssim 0.1$ Hz) is typically in the order of microns at the surface and submicrons for underground. As the main contribution to the RMS amplitude is concentrated in the low frequency band ($\lesssim 1$ Hz), the resonant peaks of the mechanical system in this frequency region must be suppressed. The microseismic peak around 0.1-0.3 Hz contributes to most of the seismic RMS amplitude, therefore we try to place the mechanical resonances away from this region. In underground locations, the microseismic motion itself is largely coherent across the entire interferometer, therefore it would be of little ill effect on the interferometer stability. The actual problem is that the resonances of the seismic isolation chains can be excited with different and varying phases, thus resulting in large relative motions of the interferometer mirrors. Therefore the resonances of the seismic attenuation chains must be strongly damped.

Passive Damping

There are fundamentally two ways of damping the mechanical resonances: passive and active damping. Passive damping can be achieved by adding a viscous damper which outputs a braking force proprtional to the relative velocity between the damper and the object to be damped. Figure 2.7 shows a conceptual design of a viscously damped mechanical oscillator. The equation of motion of the system is written as

$$M\ddot{x} = -k(x - x_0) - \gamma(\dot{x} - \dot{x}_0), \tag{2.4}$$

where γ is the damping coefficient of the damper. This damping adds to that from the internal friction of the flexure's material, which is expressed as a loss angle. Because the structural damping contribution is typically smaller wherever a damper is implemented, it is normally neglected in simulations.
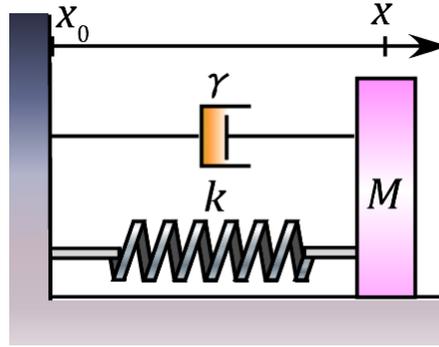
Figure 2.7: A mechanical oscillator with viscous damping.

From the Fourier transform of this equation, the frequency response of the suspended mass to the ground vibration is calculated as

$$H(\omega) = \frac{1 + 2i\eta(\omega/\omega_0)}{1 + 2i\eta(\omega/\omega_0) - (\omega/\omega_0)^2}, \tag{2.5}$$

where the damping ratio η is given by $\eta = \gamma/2M\omega_0$. A system with dissipation is often characterized by a quality factor of the resonance, which is given by

$$Q = \frac{1}{2\eta}. \tag{2.6}$$
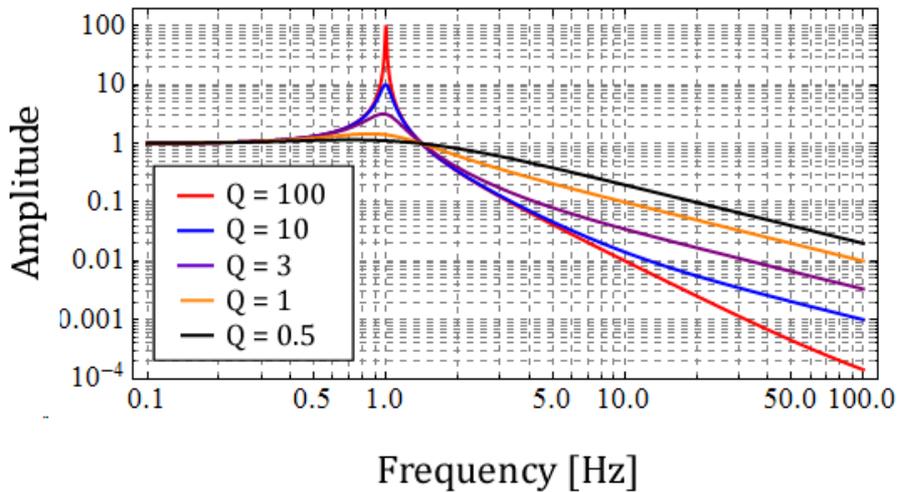
Figure 2.8: The amplitude of the transfer function of a viscously damped mechanical filter with various quality factors.

The amplitude of the transfer function $H(\omega)$ with various quality factors is plotted in Figure 2.8. There are two important characteristics in the transfer function of the viscously damped system. First, the height of the peak at the resonance ($f = f_0$) gets smaller when the damping gets stronger, and is roughly equal to Q. Second, the amplitude of the transfer function rolls off in proportion to only f^{-1} above the frequency Qf_0, instead of

f^{-2} observed in the system with no dissipation. Thence the performance of the mechanical filter is degraded at high frequencies in viscously damped system.

The performance degradation can be avoided by isolating the damper from the ground vibration by means of another mechanical filter as shown in Figure 2.9. This technique is called *flexible damping*. Although the additional spring introduces another damped resonance to the system, the ampitude of the transfer function falls in proportion to f^{-2} at high frequencies like in the case with no damping (Figure 2.10).
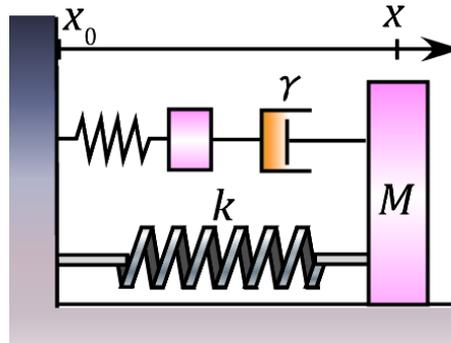
Figure 2.9: A mechanical oscillator with flexible damping.
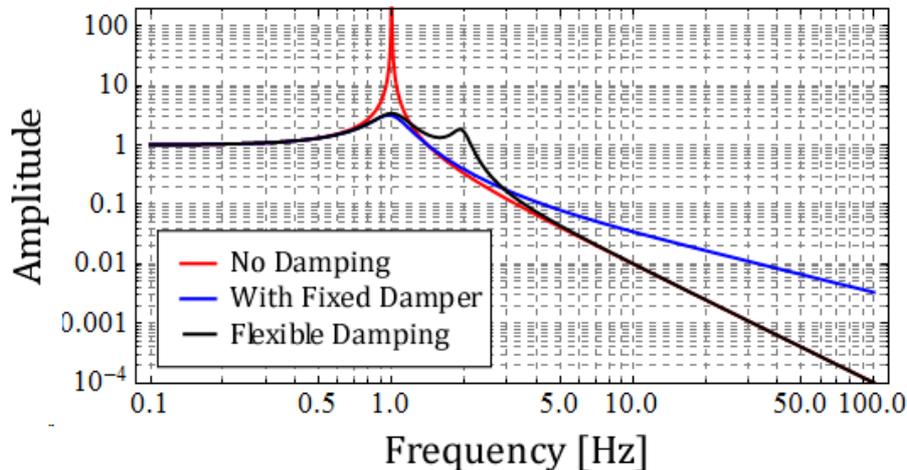
Figure 2.10: Comparison of the transfer functions of the mechanical filter with no damper, a fixed damper, and a flexibly supported damper.

A simple way to implement passive damping in the suspension system is the use of an eddy current damper [31], which is composed of permanent magnets on the damper acting on and conductive objects placed on the oscillator to be damped. When a conductive material experiences a time-varying magnetic field, eddy currents are generated in the conductor. These currents generate a magnetic field with opposite polarity of the applied field and a delay due to the induced field decay, causing a resistive force. Suspension systems with eddy current dampers have been developed for TAMA [32].

Active Damping

The use of passive damping has advantages such as low cost, robustness, low complexity and ease of implementation. However, eddy currents are proportional to the relative velocity, i.e. to the frequency of the oscillator. Therefore it is difficult to design the passive dampers so that the resonaces of all the translational/rotational motions of the suspended mass are damped sufficiently. In addition, suspension systems with eddy current dampers suffer from severe thermal noise at high frequencies, therefore one cannot use them near the optics of the interferometer.

In active damping systems, the vibration of the suspended mass is suppressed by feedback controls with vibration sensors and actuators. The active damping strength can be tuned flexibly and the frequency response can be controlled by designing the servo filters. If one places sensors and actuators with sufficient numbers and proper configuration, the motion of the suspended mass can be controlled in all traslational/rotational DoFs individually. The servo filters of the feedback controls have to be designed carefully so that they do not inject the sensor, actuator and electric circuit noise in the form of random motion of the suspended mass. An advantage of active damping is that, after damping the unwanted oscillations it can be switched off, thus eliminating its actuation noise.

Chapter 3

Vibration Isolation Systems for LCGT

3.1 General Consideration

Seismic isolation of the optics in LCGT is accomplished by the vibration isolation systems which must possess the following features:

- Passive attenuation capability to suppress the seismic noise level well below the gravitational wave signal level other noises levels at the frequency of > 10 Hz).

- Suppressing the RMS amplitude of the mirror displacement and velocity at all lower frequencies (< 10 Hz) to below 0.1 μm or μm/s to achieve fast lock acquisition and stable operation of the interferometer.

- UHV (Ultra-High Vacuum) compatibile.

The specific LCGT requirements for the amplitude of the mirror motion displacement (in the longitudinal direction) are summarized in Table 3.1. Besides the seismic noise, the sensitivity of the interferometer around 10 Hz is mainly limited by the radiation pressure noise and the suspension thermal noise. Our goal is suppressing the seismic noise level well below these noise levels at 10 Hz and higher frequency. More specifically, the requirement for the seismic noise level is to be lower by a factor of 10 than these noise levels at 10 Hz and rolling off more steeply than f^{-2}. The test mass displacement due to the thermal noise is esitemated as 2×10^{-19} m/$\sqrt{\text{Hz}}$ at 10 Hz and the radiation pressure noise is 3×10^{-19} m/$\sqrt{\text{Hz}}$ (in the broad-band RSE configuration), therefore the requirement on the test mass displacement due to seismic motion becomes 3×10^{-20} m/$\sqrt{\text{Hz}}$ at 10 Hz.

The motions of the auxiliary optics, such as the beam splitter and recycling mirrors, also affect the sensitivity of the interferometer due to the couplings in the sensing and control schemes of the interferometer, but to a much lower extent than the test mass. Figure 3.1 shows the maximum permitted displacements of the beam splitter and recycling mirrors such that these dislacement noises do not exceed the target sensitivity of the interferometer. The requirement for the longitudinal displacement of auxiliary mirrors is set a factor of 10 lower than these levels.

	Spectrum Density at 10 Hz
Test mass (TM)	3×10^{-20} m/$\sqrt{\text{Hz}}$
Beam splitter (BS)	5×10^{-17} m/$\sqrt{\text{Hz}}$
Power recycling mirror (PRM)	5×10^{-15} m/$\sqrt{\text{Hz}}$
Signal recycling mirror (SRM)	1×10^{-16} m/$\sqrt{\text{Hz}}$

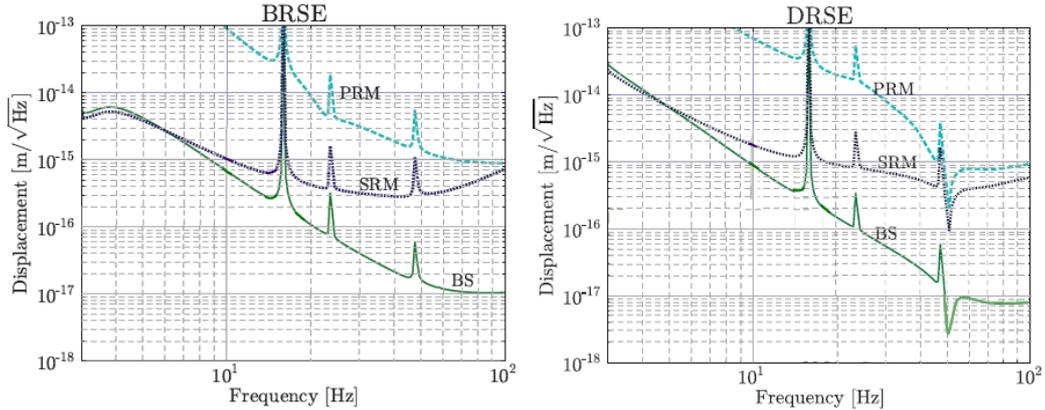Table 3.1: Requirement for the longitudinal displacement of each mirror.

Figure 3.1: The maximum permitted displacement of the auxiliary mirrors [33], in the case of the broad-band RSE (left) and the detuned RSE (right) configuration.

As described in chapter 2, 0.1-1% of the vertical motion is transferred to the longitudinal direction by mechanical cross-couplings, therefore vertical seismic attenuation is also required. Even without mechanical couplings, the vertical motion is coupled to the longitudinal direction at least by 0.3% in LCGT. This coupling comes from the fact that the interferometer is not constructed in the horizontal plane, for the practical reason. As there are many groundwater sources in the Kamioka mine, one needs to flow the water outside the tunnel and therefore the interferometers is constructed in a tunnel with tilt of 1/300.

The required RMS displacement and velocity of the test mass motion, integrated down to 100 mHz, are set as 0.1 μm and 0.1 μm/s respectively.

3.2   System Overview

In order to meet the requirements described above, the vibration isolation system for LCGT will be based on the Seismic Attenuation System (SAS), which has been developed for TAMA and LIGO [34, 35]. The conceptual designs of the vibration isolation systems are illustrated in Figure 3.2. Each stage is composed by a horizontal pendulum and a vertical spring oscillator for balanced and progressive attenuation in all degrees of freedom (DoFs). Type-A system will be used for the test masses and type-B system will be used for the beam splitter and the recycling mirrors (Figure 3.3).

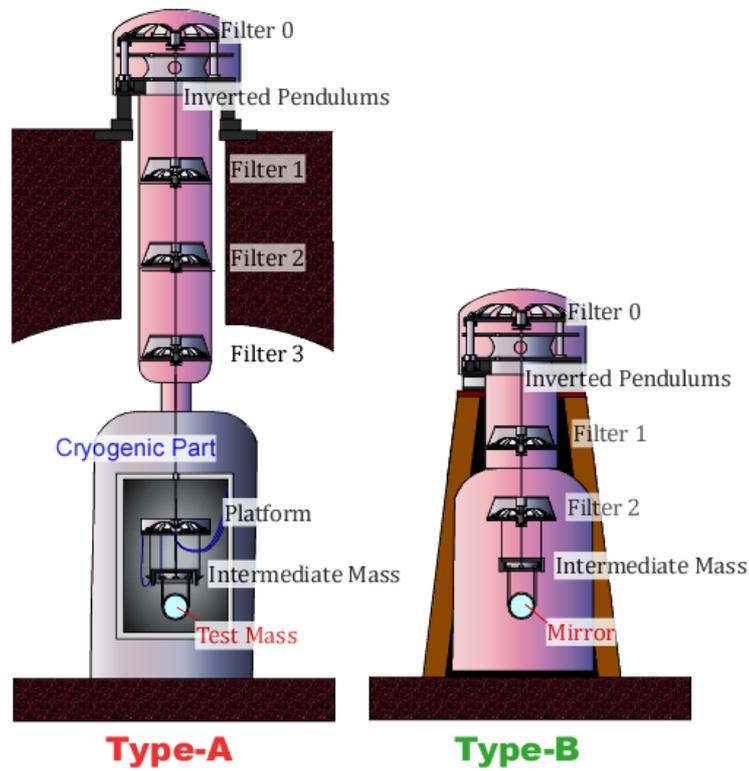The vibration isolation system is divided into three parts:

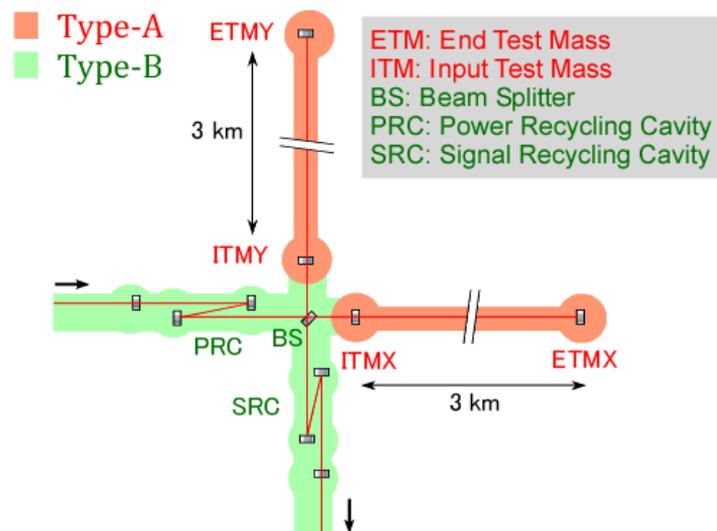Figure 3.2: Conceptual design of the vibration isolation systems in LCGT.

Figure 3.3: The optical configuration of the main interferometer part of LCGT and disposition of the vibration isolation systems.

1. The pre-isolation and static-control stage at the top of the chain. It is designed to reduce the mirror RMS movements below the requirements to allow for lock acquisition.

2. The chain of mechanical filters to achive the required seismic attenuation both in the horizontal and the vertical directions. It provides the bulk of the seismic attenuation.

3. The mirror suspension system as an interface between the mechanical filters and the core optics of the interferometer. It provides the control forces and sensing for interferometer locking.

Although there is no actual physical separation, the first and second parts are conventionally known as SAS, and the last part is known as the *payload* of the seismic attenuation chain.

In the type-A system, the pre-isolation stage sits directly on the floor of the upper tunnel, to take an advantage of the rock's stability. The attenuation chain resides inside the 1.2 m diameter borehole, and the mirror suspension system and its cryostat reside in a separate chamber in the lower tunnel. In the type-B system, the pre-isolation stage sits on the external support structure enveloping the attenuation chain.

Pre-isolation Stage

This stage is in charge of seismic attenuation starting from $f \sim 0.1$ Hz and f and static-control of the suspension point position and yaw orientation of the chain. Figure 3.4 shows the schematic design of the pre-isolator. The stage is supported from the ground or the support structure by three Inverted Pendulums (IPs), which provide seismic attenuation in the horizontal plane. At the top of the stage, there is a large Geometric Anti-Spring (GAS) filter for vertical seismic attenuation. It is twice as large in diameter as the standard GAS filter used in the attenuation chain, and called the top filter. In order to achieve seismic attenuation at the microseismic peak (100-300 mHz) and reduce the RMS amplitude of the mirror displacement, the IPs and top filters will be tuned at resonant frequencies lower than 100 mHz. The working principle of the IP and GAS filter will be explained in the next section.

The horizontal motion of the stage will be controlled by the use of three single-axis accelerometers [36], three Linear Variable Differential Transformer (LVDT) position sensors [37] which measure the relative motion of the stage with respect to an external frame fixed to the ground, and three coil-magnet actuators [38]. The design of the control system is essentially same as developed for and used in TAMA-SAS and Virgo [39, 40].

Standard GAS Filter

In order to achieve required seismic attenuation both in horizontal and vertical directions, a chain of standard GAS filters will be suspended from the pre-isolation stage. Each GAS filter is suspended by a single wire, and its suspension points are placed nearby its center of mass (Figure 3.5). In this configuration, the motion of the filter is attenuated in every translational and rotational DoF. The cantilever blades and the suspension wires are made of maraging steel [41], which has particularly good creep characteristic [42].

Figure 3.4: The 3D drawing of the pre-isolator.

Figure 3.5: The schematic design of the standard GAS filter

Mirror Suspension System (Payload)

This part is located at the very bottom of the attenuation chain. It plays a role to precisely control the mirror position and orientation and provide additional seismic attenuation. As they hold directly the mirrors of the interferometer, suspensions must be carefully designed so that they do not generate thermal noise or acoustic emission noise above the acceptable level.
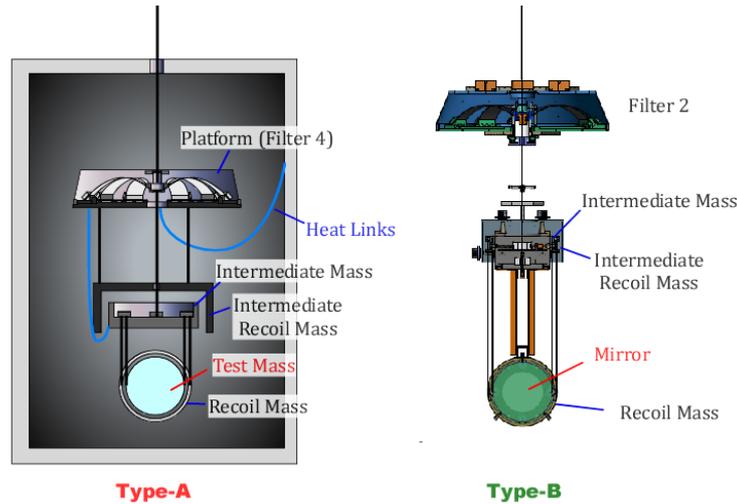

Figure 3.6: The conceptual designs of the mirror suspension systems in type-A and type-B vibration isolation systems.

Figure 3.6 shows the conceptual designs of the suspension systems in type-A and type-B systems. In both cases, an intermediate mass is suspended by a single wire from the upper stage, and the mirror and its recoil mass are suspended from the intermediate mass by four wires each. The control force and torque are exerted onto mirrors from the coil-magnet actuators on its recoil mass. A recoil mass hanging from the bottom GAS filter is added to provide control actuation to the intermediate mass. A two level control is necessary because only very delicate forces can be applied on the mirror, while larger authority can be applied on the intermediate mass without fear of injecting excessive control noise.The concept of using a recoil mass (reaction mass) hung in parallel to the mirror suspension was introduced in Virgo last stage suspension system [43] and adopted in TAMA [44]. There are several technical advantages of using a recoil mass:

- The actuator is isolated from seismic disturbance, and therefore the fluctuation of the actuation efficiency due to the change of the relative position between the mirror and actuation mass is suppressed.

- The actuation on the mirror is isolated from the upper stages, because the reaction from the mirror and the recoil mass compensate each other at the intermediate stage. It simplifies the servo design for the mirror actuation.

The recoil mass for the intermediate mass is equipped with actuators and position sensors to control the motion of the intermediate mass. In type-B system, Optical Sensor and

Electro-Magnetic actuator (OSEM) [45], which has been developed for advanced LIGO, will be used for the position sensing and actuation.

In type-A system, the suspension system is cooled down at cryogenic temperature to reduce the thermal noise. In order to transfer the heat absorbed in the mirror from the laser beams, the test mass is suspended by four sapphire fibers with 1.6 mm thickness and 30 cm length. The heat is transfered from the intermediate mass to the upper stage (platform), and then finally transfered to the inner shield of the cryostat via heat links made of pure aluminum. Since the heat link wires are mechanically connected to the cryostat, which is firmly fixed to the ground, extra vibration from the cryostat may be introduced to the suspension system through the heat links. This problem will be studied later.

3.3   Mechanical Filters

3.3.1   Inverted Pendulum (IP)

An inverted pendulum (IP) is a horizontal isolator with low resonant frequency (below 50 mHz). It provides seismic attenuation at the microseismic peak (100-300 mHz) by one order of magnitude and a soft way to set the position of the entire system in the horizontal directions. A simple model of the IP is shown in Figure 3.7. The IP consists of a flex joint fixed to the ground, a rigid cylindrical leg connected onto it, and a mass on the top of the leg. When the mass is displaced from the vertical position, a restoring force acts on it with an effective spring constant

$$k_\mathrm{eff} = \frac{k_\theta}{l^2} - \left(\frac{m}{2} + M\right) \times \frac{g}{l}. \tag{3.1}$$

Here, k_θ is the torsional spring constant of the flex joint, M is the mass of the payload, m is the mass of the leg, and l is the length of the IP. The first term of k_eff corresponds to the elastic restoring force of the flex joint, while the rest represents a repulsive force, called *gravitational anti-spring force*. With the gravitational anti-spring effect, the effective spring costant of the IP k_eff can be easily reduced by increasing the mass of the payload.

In the case of real IPs, inelastic damping effect due to the internal friction of the flex joint must be taken into account. Introducing an imaginary part with an intrinsic loss angle ϕ to the torsional spring constant, the effective spring constant becomes

$$k'_\mathrm{eff} = \frac{k_\theta}{l^2} \times (1 + i\phi) - \left(\frac{m}{2} + M\right) \times \frac{g}{l}. \tag{3.2}$$

One can define the equivalent loss angle of the effective spring constant as

$$\phi_\mathrm{eff} = \frac{k_\theta}{l^2 k_\mathrm{eff}} \phi. \tag{3.3}$$

Therefore the quality factor of the IP resonance decreases with the effective spring constant of the IP. This is an important and useful property of the IP, because an IP tuned at sufficiently low frequency needs no external damping. Figure 3.8 shows the measured quality factor with the resonant frequnecy of the IP which has been developed for LIGO. The
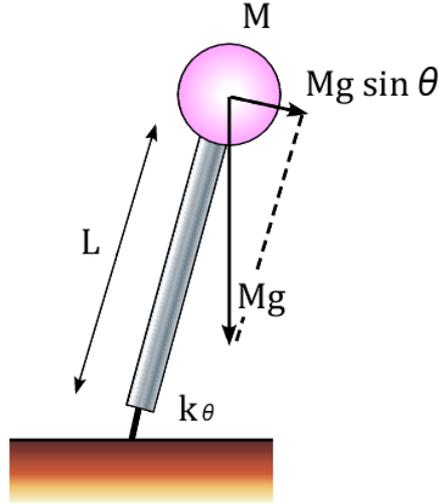
Figure 3.7: The schematic view of the IP.

downside of this loss mechanism is that when the IP is tuned at extremely low frequency and the quality factor approaches to $Q \sim 1$, the IP shows hysteretic behaviors. Therefore in most cases the IP is tuned at not lower than 30 mHz when it is used as a seismic isolator in gravitational wave detectors. This limits the attenuation of the microseismic peak (at 100-300 mHz) to a factor between 10^{-1} and 10^{-2}.
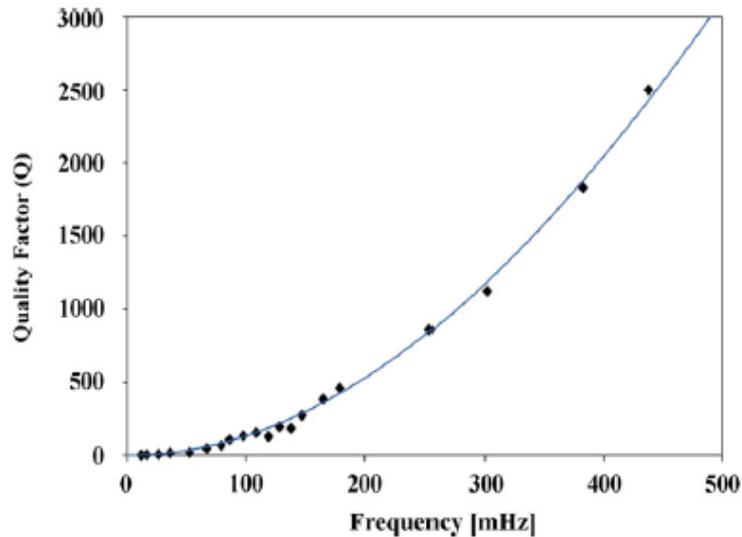

Figure 3.8: Measured quality factor versus resonant frequency of the HAM-SAS IP developed for LIGO [46].

The frequency response of the IP from the ground motion is written as [34]

$$H_{\mathrm{IP}}(\omega) = \frac{A - B\omega^2}{A - \omega^2}, \tag{3.4}$$

where

$$A = \frac{k_{\text{eff}}}{M + \frac{m}{4} + \frac{I}{l^2}}, \quad B = \frac{\frac{m}{4} - \frac{I}{l^2}}{M + \frac{m}{4} + \frac{I}{l^2}}. \tag{3.5}$$

Here I represents the moment of inertia of the leg. Figure **??** shows the amplitude of $H_{\text{IP}}(\omega)$ as a function of frequency. The IP transfer function saturates at the high frequency, due to the coefficient B in the transfer function (**??**). This behavior is physically related to the *Center of Percussion (CoP) effect* [47, 34]. To reduce the CoP effect the IP legs should be made as light and as short as possible. In order to further compensate the CoP effect, the mass distribution of the leg can be changed by introducing a counter weight at the bottom of the leg (Figure 3.10).
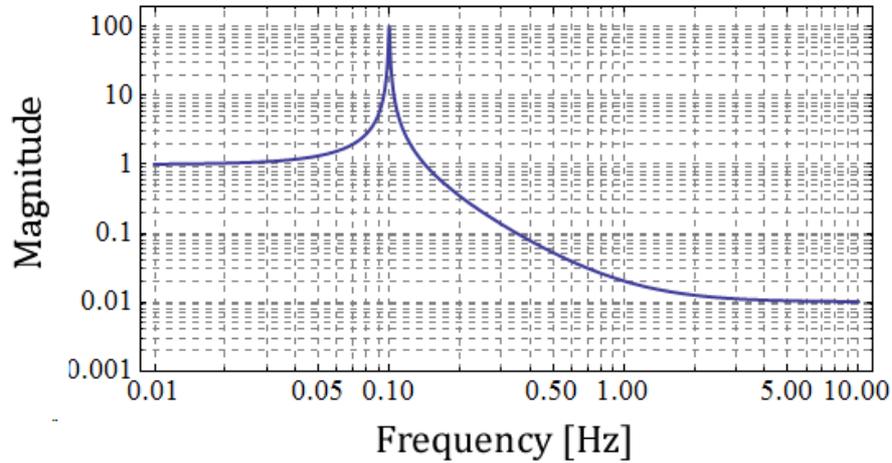

Figure 3.9: The transfer function of an IP with the resonant frequnecy of 0.1 Hz and the saturation level of 10^{-2}.

The IP used in LCGT is essentially a copy of the HAM-SAS IP, which has been developed for advanced LIGO [35]. The leg of the IP is an aluminum pipe with 1 mm thickness and ~ 50 cm length. Due to the lightness of the leg, the CoP effect is mitigated and the attenuation performance saturate at $\sim 10^{-3}$ without couter weights and at $10^{-5} \sim 10^{-4}$ with them.
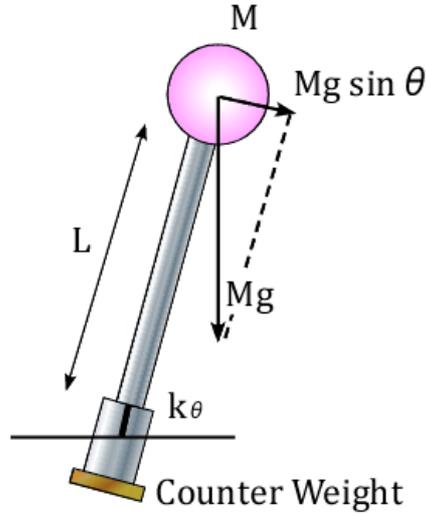
Figure 3.10: The schematic view of the IP with the counter weight mounted at the bottom of the leg.

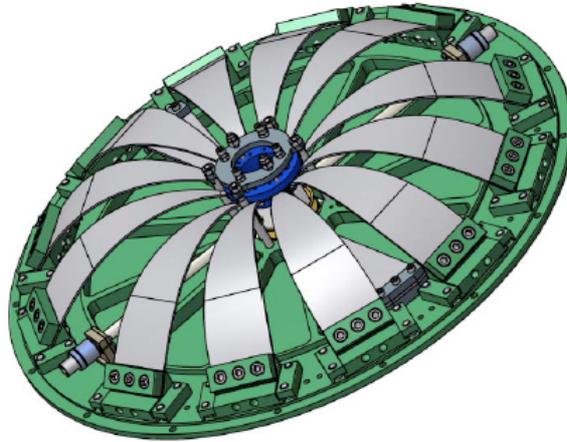## 3.3.2   Geometric Anti-Spring (GAS) Filter

Figure 3.11: The schematic view of the GAS filter.

The GAS filter consists of a set of radially-arranged cantilever blades clamped on the base frame and to the central disk called the *keystone* (Figure 3.11). The blades are flat when they are manufactured and bend like fishing rods when they are loaded. The working principle of the GAS filter is mathematically described in Ref. [48], while its behavior can be understood by means of a simple analytical model shown in Fig. 3.12. In this model, a cantilever spring is represented as a combination of vertical and horizontal linear springs. Due to the symmetry of the system, one can simplify the model to a single blade model with the constraint that the tip of the blade moves only along the vertical axis.

The payload of mass M is suspended by a vertical spring of elastic constant k_y and a
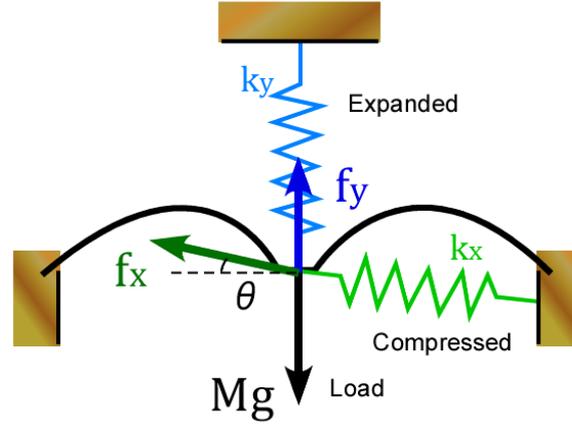
Figure 3.12: An analytical model of the GAS spring.

horizontal spring of elastic constant k_x. The angle formed by the horizontal spring and the horizontal axis θ is zero when the tip of the blade is at the equilibrium position $(y = y_{eq})$. Then the equation of motion in the vertical axis is written as

$$M\ddot{y} = -k_y(y - y_{eq}) - k_x(l - l_{0x})\sin\theta, \tag{3.6}$$

where l is the actual length of the horizontal spring and l_{0x} is its natural length. Expanding the equation of motion around the working point y_{eq} to the first order of y, one obtains the following linearized equation of motion:

$$M\ddot{y} = -\left[k_y - \left(\frac{l_{0x}}{x_0} - 1\right)k_x\right](y - y_{eq}) = -k_{eff}(y - y_{eq}). \tag{3.7}$$

Here x_0 is the horizontal distance between the central keystone and the support point of the horizontal spring. When the horizontal spring is under compression $(x_0 < l_{0x})$, it causes a repulsive force in the vertical direction and therefore the effective spring constant is reduced from the spring constant of the vertical spring $(k_{eff} < k_y)$. This is the principle of the anti-spring effect in the GAS springs. The name of Geometric Anti-Spring stands for the fact that the anti-spring is realized by a specific geometry of the cantilever blade.

The effective spring constant and the resonant frequency can be reduced by increasing the compression of the blades (decreasing x_0). When the GAS filter is tuned toward lower resonant frequencies, its quality factor decreases progressively, as observed in the IP. Figure 3.13 shows the measured quality factor and resonant frequency of the GAS filter. The quadratic behavior due to the structural damping is observed at lower frequenies, while a dramatic deviation appears at the frequencies above 200 mHz. The transition from quadratic behavior at low frequency to the exponential behavior at high frequencies can be explained by the Self Organized Criticality (SOC) of the dislocation, which is detailed in Ref. [49].

The transfer function of the GAS filter from the vertical displacement of the frame to that of the keystone is written in the same form as that of the IP (eq. (3.4)). Due to the CoP effect, the attenuation performance saturates at high frequencies and is typically limited to $\sim 10^{-3}$. It can be compensated by adding a wand with a counter weight in parallel to the blades, called the *magic wand* (Figure **??**), which allows to improve the attenuation saturation up to 10^{-4}. [**?**].
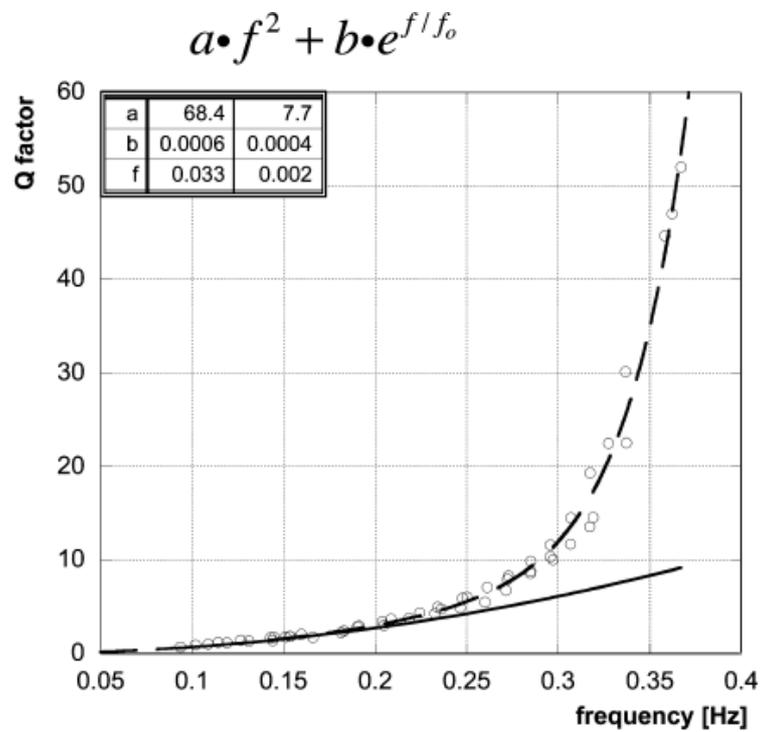
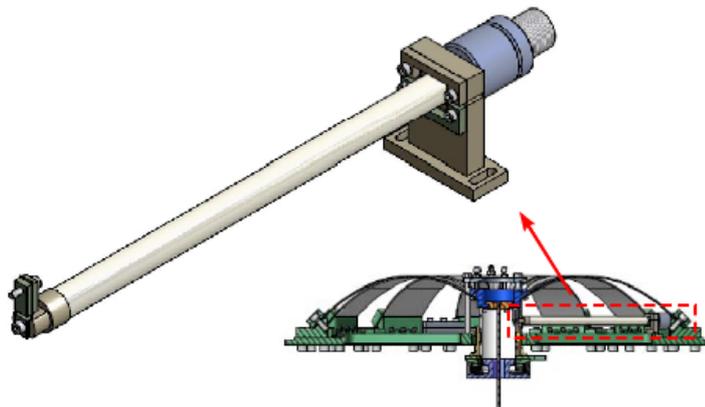Figure 3.13: Measured quality factor versus resonant frequency of the standard GAS filter for LCGT [49].

Figure 3.14: The magnc wand used to compensate the CoP effect.

Chapter 4

Rigid-Body Modeling of Vibration Isolation Systems

4.1 Modeling of Mechanical Systems

In order to estimate the expected performance of a vibration isolation system and design it, one needs to construct a mechanical model of it. There are fundamentaly three kinds of models: the point-mass model, rigid-body model and elastic-body model. The following figure shows the conceptual diagram of them.
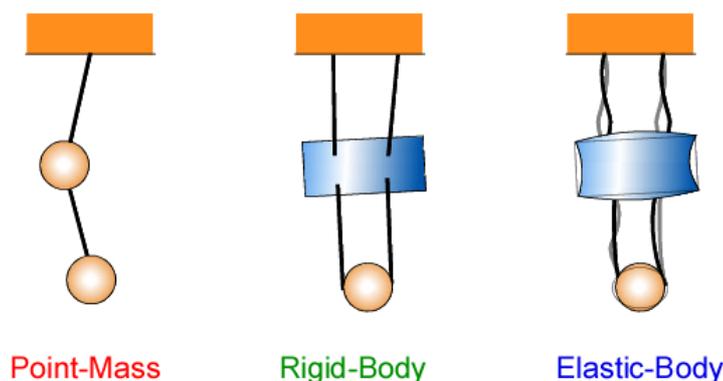
Figure 4.1: Conceptual diagram of three kinds of models.

In the point-mass modeling, the vibration isolation system is assumed to be a group of point masses which are connected by ideally elastic elements with well defined bending points, effectively coincident with the center of mass. Since it is very simple and easily constructed, we often use this model to roughly estimate the attenuation performance and study the control strategy. However, this model is fundamentally uni-dimensional, therefore the cross-talks between other degrees of freedom (DoFs) cannot be taken into account. Especially, the rotational motions of an object are easily excited by the coupling from the translational motion due to mechanical imperfections and misalignments, so that it is difficult to evaluate the transmittion of rotational motions to the mirror by this simple model.

In the rigid-body modeling, one regards the vibration isolation system as a combination of rigid bodies with mass and moment of inertia and elastic elements connecting with them. Each rigid-body has six DoFs, three for tralslation and three for rotation, and it is possible to consider the cross-talks between DoFs in the rigid-body models. However, since many DoFs have to be taken into account, more complicated foamulae are required for the calculation. The Rigid-body approximation is valid at only low frequencies ($f \lesssim 50$ Hz for our systems), thence we need to keep in mind that the predicted performance of the vibration isolation system can be degraded to some extent at at and around the internal resonant frequencies of the "rigid" bodies that become elastic elements. Above the "rigid" body resonances, additional attenuation performance appears. Unfortunately this additional attenuation is normally superfluous, and only the negative effects from the internal resonances are relevant for seismic attenuation design. When designing a seismic attenuator unit, one always strives to have as high as possible internal resonances and, if inconveniently low internal resonances are unavoidable, the designer needs to damp them appropriately. This requires estimation of the interna modes of allcomponents.

In order to calculate the dynamics of mechanical systems in the high frequency region, one needs elastic-body models, in which the mass and elasticity distributions of the components are taken into account. Since analytical approaches are only valid for quite simple systems, we often use Finite Element Method (FEM) for this calculation. In this method, matrix calculation of huge size are required. Therefore, the elastic-body modeling can be adopted only for small subsystems. This is normally adequate because these calculations are normally performed to verify that there are no relevant "low" frequency resonances. If a relevant resonance is identified, it can either be eliminated by stiffening the component, neutralized by adding a suitable damper, or included into the rigid body simulation by means of a suitable effective spring and effective mass in the model.

So far, the estimation of the performance of vibration isolation systems in LCGT has been performed only by point-mass modeling, and the calculation with rigid-body models has not been performed yet. I construct three-dimensional rigid-body models of the vibration isolation systems and investigate the three dimensional dynamics of the vibration isolation systems. Several critical aspects of this simulation are cross checked by independent parallel simulation, until all relevant results agree. I take the occasion to thank Ettore Majorana, Eric Hennes and Ryutaro Takahashi, that performed these vital cross check for me, and taught me the ropes of the trade in the process.

4.2 Rigid-Body Modeling

4.2.1 Overview

I developed the rigid-body models of the vibration isolation systems for LCGT starting from the Mark Barton's suspension models, which he developed initially for TAMA, and then for LIGO [?, 50]. The models developed here have the following features:

- All the suspended objects are regarded as rigid bodies with up to 6 DoFs, and their internal elasticity is not taken into account.

- A wire is assumed to be a massless spring with stretching and torsional elasticity.

Since it is assumed to be massless, its violin modes are not taken into account.

- The vertical spring (GAS filter) used in the model works as an ideal linear spring with a spring constant and a single working-direction. The saturation of the attenuation performance due to center of percussion effect is considered.

- The dissipation due to the internal friction of the elastic material is taken into account. Thence the spring constants of the vertial springs and wires have imaginary parts with finite loss angles, which are assumed to be constant over all the frequencies (structural damping).

With the assumption described above, the potential, damping and kinetic energies are calculated from the physical parameters and geometry of the mechanics, and then equations of motion of the systems are derived from the Lagrangian equations. Since the calculation includes compricated formula manipulation, a symbolic mathematics package *Mathematica* version 7.0 is used for the calculation.

The calculation provides engenfrequencies and eigenmodes of the system, and various transfer functions which represent the performance of the vibration isolation systems and give the information about their controlability. In the following sections, I will explain how to calculate them from the given mechanical models and parameters.

4.2.2 Coordinate System

The coordinate system used in the model is defined in Figure 4.2. We define the horizontal axis parallel to the laser beam in the interferometer (longitudinal direction) as z-axis, the horizontal axis perpendicular to the beam (transversal direction) as x-axis, and the vertical axis as y-axis. The rotations about the x, y and z-axis are called "pitch", "yaw" and "roll" respectively. These names for the rotations are taken from nautical terminology.
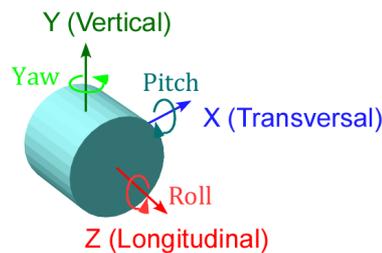

Figure 4.2: Coordinate system used in the model.

The position and orientation of each object are defined by the use of the six coordinates $(x, y, z, \theta_x, \theta_y, \theta_z)$. Rotations are not commutative, therefore the orientation of the object depends on the order of rotations. I choose the following rotation sequence in the simulation: the first rotation is the pitch angle about x-axis, the second is the yaw angle about y-axis, and the third is a roll angle about z-axis (Figure 4.3).

The coordinate system defining the position of the objects is called *global* coordinate system. When setting up a mechanical model, however, it is convenient to use a coordinate
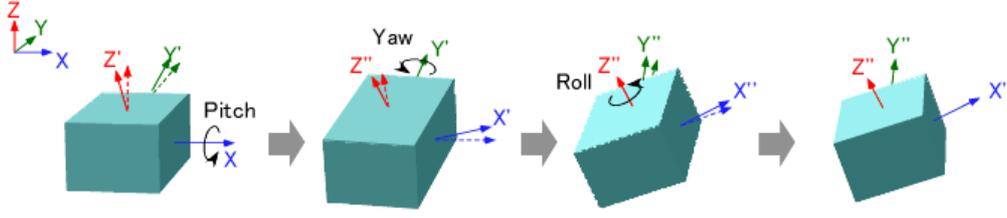
Figure 4.3: The rotation sequence defining the orientation of the object.

system which is fixed to the object and originates at its center of mass. This is called *local coordinate system*.

Since the suspension point of a wire is a fixed points on the objects it attaches to, we often express it by the use of local coordinate system. When we calculate the elastic potential energy stored in the wires, however, we need to know the global coordinate of the suspension point from the given local coordinate (x_b, y_b, z_b). The global coordinate (x_s, y_s, z_s) can be calculated as

$$
\begin{pmatrix} x_s \\ y_s \\ z_s \end{pmatrix} = \begin{pmatrix} x \\ y \\ z \end{pmatrix} + \begin{pmatrix} \cos\theta_z & -\sin\theta_z & 0 \\ \sin\theta_z & \cos\theta_z & 0 \\ 0 & 0 & 1 \end{pmatrix} \cdot
$$
$$
\begin{pmatrix} \cos\theta_y & 0 & \sin\theta_y \\ 0 & 1 & 0 \\ -\sin\theta_y & 0 & \cos\theta_y \end{pmatrix} \begin{pmatrix} 1 & 0 & 0 \\ 0 & \cos\theta_x & -\sin\theta_x \\ 0 & \sin\theta_x & \cos\theta_x \end{pmatrix} \begin{pmatrix} x_b \\ y_b \\ z_b \end{pmatrix}. \quad (4.1)
$$

Here $(x, y, z, \theta_x, \theta_y, \theta_z)$ represent the position and orientation of the attached body.

4.2.3   Potential Energy Terms

Wires

The potential energy of each wire is separated into two terms: stretching and torsional potential energies. The first one refletcs the increase of the straight-line distance between its two attachment points:

$$
U_{\mathrm{wires}} = \frac{1}{2} k_{\mathrm{w}} (l(\boldsymbol{x}) - l_0)^2. \quad (4.2)
$$

Here l_0 is the natural length of the wire and $l(\boldsymbol{x})$ is the actual distance between two attachment points, which is parameterized by the position and orientation of the two objects. k_{w} is the elastic constant of the wire, which depends on the shape of the wire and Young's modulus E of the material. The elastic constant of the wire with a constant cross section S and the length l_0 is given as

$$
k_{\mathrm{w}} = \frac{ES}{l_0}. \quad (4.3)
$$

Wires with variable cross section have to be suitably taken into account.

The second term, the torsional potential energy, provides relatively small restoring force to the suspended object. Its effect is negligible when the object is suspended by more than one wire, while it plays an important role in the single wire suspension. The potential term is written as

$$U_{\text{wiret}} = \frac{1}{2} k_{\text{t}} \Delta \theta_{\text{t}}^2, \tag{4.4}$$

where $\Delta \theta_{\text{t}}$ and k_{t} represent the twist angle and the torsional stiffness of the wire. The torsional stiffness of the wire with the length l_0 and shear modulus G is given as

$$k_{\text{t}} = \frac{JG}{l_0}. \tag{4.5}$$

Here J is the polar moment of inertia of the wire cross section. In the case of circular and constant cross section with the diameter d, it is given as $J = \pi d^4 / 32$. Since the torsional stiffness of the cylindrical-shaped wire is proportional to the forth power of the wire diamter, it can be stiff easily by making its thickness large.

GAS filters

The GAS filter in the rigid-body model is assumed to be a linear and uni-dimensional spring working in the vertical direction. Since the internal resonances of the blades are much higher ($\gtrsim 100$ Hz) than the frequency of interest in the rigid-body modeling, we can neglect them; they include the transversal or rotational movement of the keystone. When the GAS filter is tuned at the resonant frequency of f_0 with the load M, the potential energy term is written as

$$U_{\text{GASF}} = \frac{1}{2} M (2\pi f_0)^2 \Delta h^2 + Mg\Delta h, \tag{4.6}$$

where Δh is the deviation of the keystone of the GAS filter from the equilibrium position. The first term provides the restoring force to the suspended object, while the second term provides a costant force that holds the keystone at its working point.

Gravitational Potential

The gravitational potential of each object is given as

$$U_{\text{gravity}} = Mgy, \tag{4.7}$$

where M is the mass and y is the global coordinate representing the vertical position of the object.

4.2.4 Kinetic Energy Terms

Bodies

When the position and orientation of an object is given as $(x, y, z, \theta_x, \theta_y, \theta_z)$, the kinetic energy about its translation is written as

$$T_{\text{translation}} = \frac{1}{2} M (\dot{x}^2 + \dot{y}^2 + \dot{z}^2). \tag{4.8}$$

On the other hand, the kinetic energy about its rotation is written as

$$T_{\text{rotation}} = \frac{1}{2}\boldsymbol{\omega}^T \boldsymbol{I} \boldsymbol{\omega}, \tag{4.9}$$

where $\boldsymbol{I}$ is the moment of inertia tensor and $\boldsymbol{\omega} = (\omega_x, \omega_y, \omega_z)$ represents the angular velocity about the local coordinate axes. Generally, $(\omega_x, \omega_y, \omega_z)$ is not equivalent to $(\dot\theta_x, \dot\theta_y, \dot\theta_z)$, because the coordinates about the rotational DoFs represents the Euler angles of the object. From the Euler angles, the angular velocity of the object is calculated as [51]

$$\begin{pmatrix} \omega_x \\ \omega_y \\ \omega_z \end{pmatrix} = \begin{pmatrix} \cos\theta_x \cos\theta_y & 0 & 0 \\ \sin\theta_x \cos\theta_y & \cos\theta_x & 0 \\ -\sin\theta_y & sin\theta_x & 1 \end{pmatrix} \begin{pmatrix} \dot\theta_x \\ \dot\theta_y \\ \dot\theta_z \end{pmatrix}. \tag{4.10}$$

Center of Percussion Effect

The attenuation performance of the GAS filters and inverted pendulums saturates at high frequencies due to their internal mass distribution. This effect can be taken into account by introducing additional terms to the kinetic energy. Consider a simple mass-spring oscillator whose kinetic and potential energies are written as

$$T = \frac{1}{2}M\dot{x}^2 + m\dot{x}\dot{x}_0, \ U = \frac{1}{2}k(x - x_0)^2. \tag{4.11}$$

M and k are the mass of the suspended object and the elastic constant of the spring, while m reflects the internal mass distribution of the spring. Thence the Lagrange equation is calculated as

$$M\ddot{x} + m\ddot{x}_0 = -k(x - x_0). \tag{4.12}$$

Due to the second term in the left-hand side of (4.12), the vibration isolation ratio at high frequencies saturates in (m/M). The saturation level of the vibration isolation ratio of GAS filter is typically $10^{-4} \sim 10^{-3}$.

4.2.5 Dissipation

Viscous Damping

There are several kinds of dissipation proccess in suspension systems. We consider two kinds of dissipation process: viscous damping which is introduced by the eddy current in conducting bodies, and structure damping due to the internal friction of elastic materials.

The damping force acting between a magnetic damper and a conducting body is proportional to their relative velocity. The damping forces of this type can be derived in terms of a function $\mathcal{F}$, which is known as the Rayleigh's dissipation function and defined as

$$\mathcal{F} = \frac{1}{2}C(\dot{x}_1 - \dot{x}_2)^2, \tag{4.13}$$

where x_1 and x_2 are the displacements of the damper and conducting body, and C is a suitable damping coefficient. Since the damping strength should be defined for each DoF, in general the dissipation function is written as

$$\mathcal{F} = \frac{1}{2}(\dot{\boldsymbol{x}}_1 - \dot{\boldsymbol{x}}_2)^T \boldsymbol{C}(\dot{\boldsymbol{x}}_1 - \dot{\boldsymbol{x}}_2), \tag{4.14}$$

where $\boldsymbol{x}_1 = (x_1, y_1, z_1, \theta_{x1}, \theta_{y1}, \theta_{z1})$ and $\boldsymbol{x}_2 = (x_2, y_2, z_2, \theta_{x2}, \theta_{y2}, \theta_{z2})$ define the position and orientation of the two objects, and $\boldsymbol{C}$ is called the damping coefficient matrix.

Structural Damping

The internal damping of the elastic elements can be expressed by adding imaginary parts to the spring constants:

$$k \to k(1 + i\phi(\omega)) \tag{4.15}$$

It is known that the loss angle $\phi(\omega)$ is roughly constant over a wide frequency band, therefore frequency-independent loss angles are used in our calculation. For the wires, we introduce a loss angle eqaul to the intrinsic loss of the materials, and for GAS filters and inverted pendulums, we introduce loss angles depending on the measured quality factor of their oscillation at the tuning resonance. It has been shown that hysteretic or even SOC controlled dissipation [ref] should be applied instead. The loss angle approximation is sufficient for the seismic attenuation design. For very low frequency oscillations and controls different and much more sophisticated simulations may be necessary.

4.2.6   Equations of Motion

The equations described above are non-linear, and difficult to be used. The Seismic attenuators work in the vanishing small movement regime, therefore equations linearized around the expected working points are perfectly suitable to evaluate the attenuator performance. The derivation of the linearlized equations of motion has conceptually the following steps:

1. Express the potential energy $U(\boldsymbol{x})$, dissipation function $\mathcal{F}(\boldsymbol{x}, \dot{\boldsymbol{x}})$, and kinetic energy $T(\boldsymbol{x}, \dot{\boldsymbol{x}})$ of the system in terms of the coordinates and the coordinate velocities.

2. Minimize the potential energy to find the equilibrium values (working points) of the coordinates $\boldsymbol{x}_{\text{eq}}$.

3. Differentiate the pontential energy of the system with respect to pairs of coordinate at equilibrium to create a matrix of second derivatives, which is known as the stiffness matrix.

$$\boldsymbol{K}: \; K_{ij} = \left. \frac{\partial^2 U(\boldsymbol{x})}{\partial x_i \partial x_j} \right|_{\boldsymbol{x} = \boldsymbol{x}_{\text{eq}}}. \tag{4.16}$$

4. In a similar way, differentiate the dissipation function and the kinetic energy with respect to pairs of coordinate velocity at equilibrium. The created matrices are called the damping matrix and the inertia matrix, respectively.

$$\boldsymbol{C}: \; C_{ij} = \left. \frac{\partial^2 \mathcal{F}(\boldsymbol{x}, \dot{\boldsymbol{x}})}{\partial \dot{x}_i \partial \dot{x}_j} \right|_{\boldsymbol{x} = \boldsymbol{x}_{\text{eq}}}, \tag{4.17}$$

$$\boldsymbol{M}: \; M_{ij} = \left. \frac{\partial^2 T(\boldsymbol{x}, \dot{\boldsymbol{x}})}{\partial \dot{x}_i \partial \dot{x}_j} \right|_{\boldsymbol{x} = \boldsymbol{x}_{\text{eq}}}. \tag{4.18}$$

5. The linearized equations of motion is written by the used of these matrices as

$$\boldsymbol{M}\ddot{\boldsymbol{x}} + \boldsymbol{C}\dot{\boldsymbol{x}} + \boldsymbol{K}(\boldsymbol{x} - \boldsymbol{x}_{\text{eq}}). \tag{4.19}$$

4.2.7 Eigenmodes

The eigenfrequencies and eigenmodes of the system can be obtained by the diagonalization of the stiffness and inertia matrices:

$$(\boldsymbol{K} - \omega_i^2 \boldsymbol{M})\boldsymbol{e}_i = 0. \tag{4.20}$$

Here $\boldsymbol{e}_i$ is the eigenvector of the i-th resonant mode and $f_i = \omega_i/2\pi$ is the corresponding engenfrequency.

4.2.8 Transfer Function

Response to Force/Torque

When one designs the control scheme of the mechanical systems by the means of sensors and actuators, it is important to know the frequency response of the system to the external and internal actuation. The transfer function from the external force/torque onto the corresponding coordinate x_i to the displacement about the coordinate x_j is calculated from the Fourier transform of the equations of motion as

$$H_{ij}^{(\mathrm{f})}(\omega) = \left[(-\omega^2 \boldsymbol{M} + i\omega \boldsymbol{C} + \boldsymbol{K})^{-1}\right]_{ij}. \tag{4.21}$$

When a suspended mass is subjected to a force/torque from its recoil mass actuator, the frequency response is calculated as a superposition of two transfer functions, from the external force/torque onto the suepended mass, and its recoil mass. The controls can either apply damping forces, to suppress resonant movement that can be excited by different causes, mainly seismic noise, or actuation control forces, to place or maintain the mass in object in the desired position.

Response to Seismic Motion

In order to calculate the frequency response to seismic motion, one needs to take into account the displacement and orientation of the ground $\boldsymbol{x}_{\mathrm{g}} = (x_{\mathrm{g}}, y_{\mathrm{g}}, z_{\mathrm{g}}, \theta_{x\mathrm{g}}, \theta_{y\mathrm{g}}, \theta_{z\mathrm{g}})$ in calculating the equations of motion. When they are included, equations of motion are written as

$$\boldsymbol{M}\ddot{\boldsymbol{x}} + \boldsymbol{C}\dot{\boldsymbol{x}} + \boldsymbol{K}\boldsymbol{x} + \boldsymbol{M}_{\mathrm{g}}\ddot{\boldsymbol{x}}_{\mathrm{g}} + \boldsymbol{C}_{\mathrm{g}}\dot{\boldsymbol{x}}_{\mathrm{g}} + \boldsymbol{K}_{\mathrm{g}}\boldsymbol{x}_{\mathrm{g}} = 0. \tag{4.22}$$

Thence the transfer function from the displacement of the ground motion $x_{i\mathrm{g}}$ to the displacement about the coordinate x_j is calculated as

$$H_{ij}^{(\mathrm{g})}(\omega) = \left[(-\omega^2 \boldsymbol{M} + i\omega \boldsymbol{C} + \boldsymbol{K})^{-1}(\omega^2 \boldsymbol{M}_{\mathrm{g}} - i\omega \boldsymbol{C}_{\mathrm{g}} - \boldsymbol{K}_{\mathrm{g}}))\right]_{ij}. \tag{4.23}$$

4.2.9 Suspension Thermal Noise

From the fluctuation-dissipation theorem, the power spectrum of the thermal fluctuation of the mirror posotion is calculated from the following formula [52]:

$$\tilde{x}_{\mathrm{therm}}^2(\omega) = -\frac{4k_B T}{\omega}\mathrm{Im}[H_{\mathrm{mirror}}(\omega)]. \tag{4.24}$$

Here k_B is the Boltzmann constant, T is the temperature, and $H_{\mathrm{mirror}}(\omega)$ is the transfer function from the external force onto the mirror to the displacement of the mirror. This formula is valid only when the whole system is at the uniform temperature. As the temperature of the suspension system around the test mass is not uniform in LCGT, more complicated formulae will be necessary for precise estimation of the thermal noise [53, 54]. Nevertheless, because the thermal noise of the upper stages is irrelevant, and the lowest suspension will be at a more or less fixed temperature, the formula (4.24) will provide a rough estimation of the thermal noise in such a system.

4.3 Consideration on the Modeling

4.3.1 Effective Bending Point

In the modeling described above, it is assumed that a wire bends exactly at its clamping points with zero radius of curvature when the suspended mass moves transversally. In reality, however, a wire bends with finite radius of curvature at the ends due to its rigidity. This radius of curvature decreases as the applied load is increased. It results in an the effective bending point along of the wire at a non-negligible distance from the nominal clamping points (Figre 4.4). This effect is due to the wire rigidity, and therefore is observed more obviously in wires of larger diameters. The distance between the clamp point and the effective bending point is calculated as [55]

$$\Delta = \sqrt{\frac{EI}{T}}, \tag{4.25}$$

where E is the Young's modulus, I is the second moment of area, and T is the tension of the wire. For a wire of circular cross section with diameter d, the second moment of area is given as $I = \pi d^4/64$.
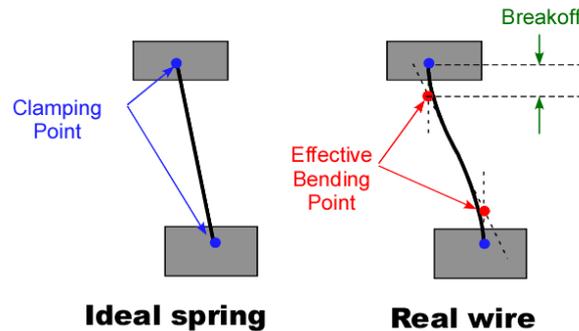

Figure 4.4: Mismatch of the clamping points and the effective bending points of the wire due to its rigidity.

In our case, the breakoff between the bending point and clamping point is in the order of mm~cm, and is much shorter than the wire lengths (~1 m). Therefore changes in the resonant frequencies of the pendulum modes due to the wire rigidity are negligible. However, the tilt modes of the suspended mass is quite sensitive to the distance between

the center of mass and the bending point, and between the mass suspension point and the point from which its payload is suspended, therefore the effect of the wire rigidity is non-negligible. In the calculation, the wire lengths and the bending points are compensated by (4.25) before calculating the potential energy.

4.3.2 Dissipation Dilution

It is well known that the loss factor of a pendulum is considerably lower than the intrinsic loss factor of the material of the wires used for the suspension. This is because most of the potential energy of a pendulum is stored in the form of lossless gravitational potential energy, and only a small part is stored in the bending of the wire. The relationship between the loss angle of the pendulum ϕ_{pen} and that of the wire ϕ_{wire} is written as [56]

$$\phi_{\mathrm{pen}} = \frac{\Delta}{2L}\phi_{\mathrm{wire}}, \tag{4.26}$$

where L is the wire length and Δ is the breakoff between the clamping point and the bending point defined in (4.25). The scaling factor $2L/\Delta$ is called the *dilution factor*.

However, in our models, the restoring force of the pendulum is caused by the elasticity of the wire, so that naively introducing the intrinsic loss angles to the elastic constant would result in overestimation of the damping (i.e. the thermal noise). In order to take into account the effect of dissipation dilution, I apply different loss factors to the horizontal and vertical movement of the supended mass. When the wire elasticity is considered in the vertical direction, the elastic potential energy is calculated as

$$U_{\mathrm{wires}} = \frac{1}{2}k_{\mathrm{w}}(1 + i\phi_{\mathrm{pen}})(l(\boldsymbol{x}) - l_0)^2 + \frac{1}{2}k_{\mathrm{w}}i(\phi_{\mathrm{wire}} - \phi_{\mathrm{pen}})(y_1 - y_2 - l_0)^2, \tag{4.27}$$

where $\boldsymbol{x}_1 = (x_1, y_1, z_1)$ and $\boldsymbol{x}_2 = (x_2, y_2, z_2)$ represent the global coordinates of the two suspension points, and $l(\boldsymbol{x}) = |\boldsymbol{x}_1 - \boldsymbol{x}_2|$.

Chapter 5

Passive Attenuation Performance

5.1 Assumption

Rigid-Body Models

In this chapter, the attenuation performances of the vibration isolation systems are estimated by means of three-dimensional rigid-body models described in chapter 4. The model contains 9 rigid bodies for type-A system and 7 rigid bodies for type-B system as shown in Figure 5.1. Since filter 0 is bound to the ground by three IPs with rigid legs, it can move only in the horizontal plane and thus it is allowed only 3 DoFs (x, z, θ_y). The other rigid bodies have 6 DoFs each, therefore the model contains 51 DoFs for type-A system and 39 DoFs for type-B system.

The parameters used in the simulation for type-A system is summarized in Figure 5.2. The cryogenic part is designed so that its total mass is fixed at 300 kg. The moment of inertia of the intermediate mass, test mass and their recoil masses is roughly estimated from the geometry shown in Figure 5.4. The wire diameters are carefully chosen so that the tensile stress of the wire does not exceed the yield tensile strength of the wire material. Note that the diameter of the sapphire fiber for the test mass suspension is determined not from the requirement on the tensile stress, but from the requirement that the fiber must be capable of transferring a sufficient amount of heat with sufficiently low temperature. The top filter and IP are tuned at resonant frequencies of 60 and 30 mHz respectively to attenuate the seismic disturbance at the microseismic peak (100-300 mHz), while the standard GAS filters are tuned at 250 mHz. The heat link wires between the radiation shield of the cryostat and the platform (PF) are assumed to be a linear spring connecting the two points. The details of the modeling will be explained later.

The parameters for type-B system is summarized in Figure 5.5. As the beam splitter (ϕ : 37 cm, L : 8 cm) and the recycling mirrors (ϕ : 25 cm, L : 10 cm) are different in dimension and mass, the parameters for their suspensions have to be different.
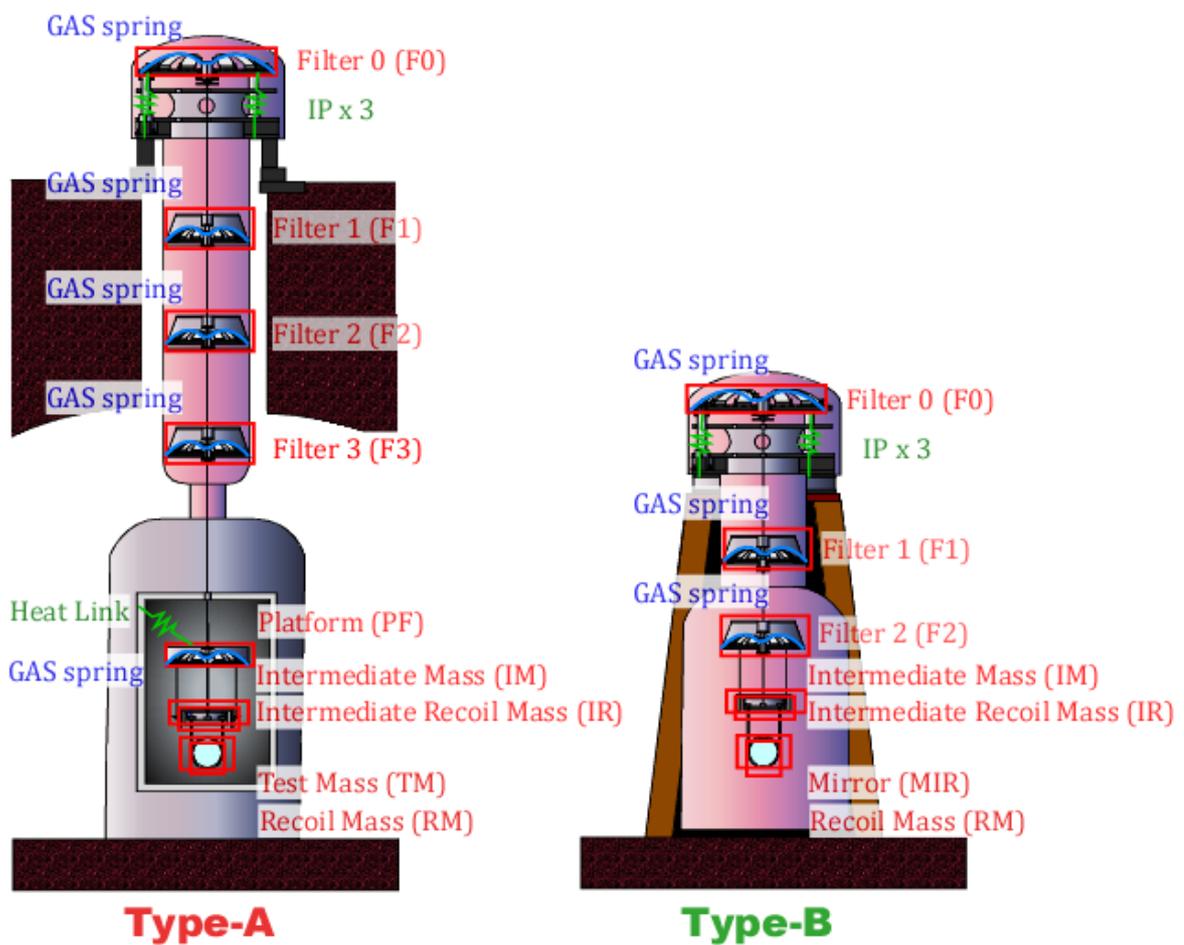
Figure 5.1: The model structure of the type-A and type-B vibration isolation systems.

description		symbol	unit	F0	F1	F2	F3	PF	IR	IM	RM	TM
body	mass	M	kg	474	90	90	90	120	60	60	37.3	22.7
	moment of inertia (x)	I_x		60	4	4	4	4	0.96	0.26	0.52	0.11
	moment of inertia (y)	I_y	kg m²	120	6.4	6.4	6.4	6.4	2.4	0.69	0.52	0.11
	moment of inertia (z)	I_z		60	4	4	4	4	1.5	0.55	0.59	0.14
wire	number of wires	n	-	-	1	1	1	1	3	1	4	4
	material	-	-	-	maraging steel			bolfur	tungsten	maraging	BeCu	sapphire
	density	ρ	g/cm³	-	8.0			7.6	19.3	8.0	8.4	4.0
	Young's modulus	E	GPa	-	195			157	411	195	136	345
	Poisson ratio	σ	-	-	0.3			0.3	0.28	0.3	0.3	0.29
	loss angle	Φ	-	-	1×10^{-3}			1×10^{-3}	1×10^{-4}	1×10^{-3}	5×10^{-6}	2×10^{-7}
	length	L	m	-	3.05	3.05	3.05	3.05	0.4	0.4	0.3	0.3
	diameter	d		-	3.1	2.8	2.5	2.2	0.6	1.4	0.7	1.6
	x-position	D_x		-	-	-	-	-	-	-	25	15
	z-position	D_z	mm	-	-	-	-	-	-	-	135	110
	radial distance to y-axis	D_r		-	-	-	-	-	-	150	-	-
	upper clamp y-position	D_{yu}		-	-5	-5	-5	-5	0	-5	0	0
	lower clamp y-position	D_{yl}		-	5	5	5	5	0	-5	0	0
GAS	resonant frequency	f_{GAS}	mHz	60	250	250	250	250	-	-	-	-
	quality factor	Q_{GAS}	-	3	6	6	6	6	-	-	-	-
	saturation level	B_{GAS}	dB	-60	-60	-60	-60	-60	-	-	-	-
IP	radial distance to y-axis	R_{IP}	mm	600	-	-	-	-	-	-	-	-
	horizontal mode frequency	f_{IP}	mHz	30	-	-	-	-	-	-	-	-
	quality factor	Q_{IP}	-	3	-	-	-	-	-	-	-	-
	saturation level	B_{IP}	dB	-70	-	-	-	-	-	-	-	-
Heat Link	stiffness (x)	k_{HLx}		-	-	-	-	5.0	-	-	-	-
	stiffness (y)	k_{HLy}	N/m	-	-	-	-	1.0	-	-	-	-
	stiffness (z)	k_{HLz}		-	-	-	-	0.8	-	-	-	-
	quality factor	Q_{HL}	-	-	-	-	-	100	-	-	-	-
	saturation level (x)	B_{HLx}	dB	-	-	-	-	-80	-	-	-	-
	saturation level (y)	B_{HLy}	dB	-	-	-	-	-90	-	-	-	-
	saturation level (z)	B_{HLz}	dB	-	-	-	-	-100	-	-	-	-

Figure 5.2: The parameters about the type-A vibration isolation systems. The definition of the geometric parameters (D_x, D_z, D_r, D_{yu} and D_{yl}) is shown in Figure 5.3
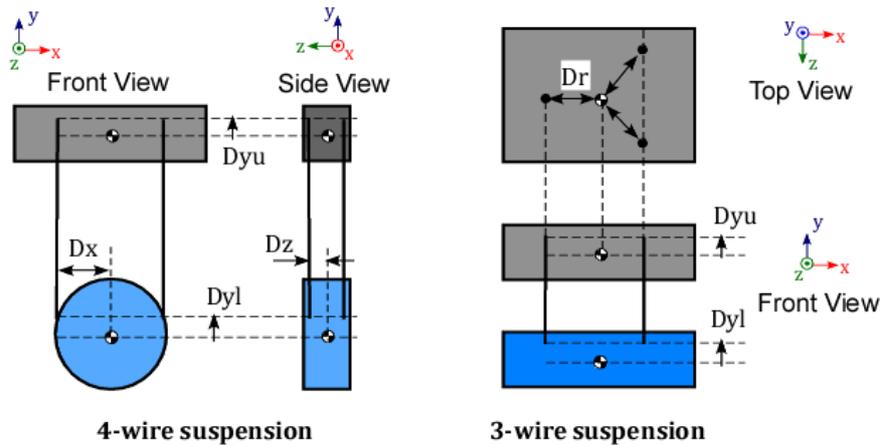

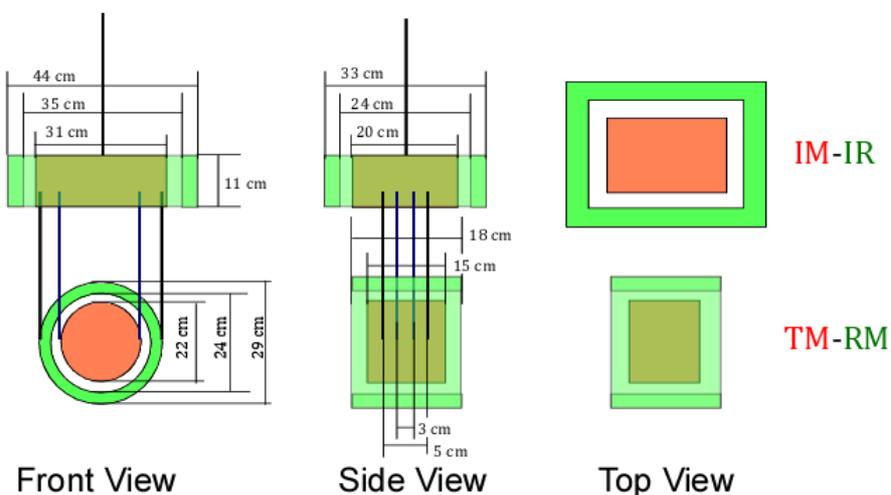Figure 5.3: Definition of geometric parameters of suspension points.

Figure 5.4: Geometry of the last stage of the type-A system assumed in the simulation.

description		symbol	unit	F0	F1	F2	IR	IM	RM	MIR
body	mass	M	kg	474	90	90	12 24	16 36	13 22	10.7 19.8
	moment of inertia (x)	Ix		60	4	4	0.25 1.0	0.15 0.60	0.18 0.30	0.051 0.19
	moment of inertia (y)	Iy	kg m²	120	6.4	6.4	0.40 1.7	0.19 0.95	0.18 0.30	0.051 0.19
	moment of inertia (z)	Iz		60	4	4	0.25 1.0	0.15 0.60	0.23 0.40	0.084 0.25
wire	number of wires	n	-	-	1	1	3	1	4	4
	material	-	-	-	maraging steel		C70-steel	maraging	tungsten	
	density	ρ	g/cm³	-	8.0		7.8	8.0	19.3	
	Young's modulus	E	GPa	-	195		200	195	411	
	Poisson ratio	σ	-	-	0.3		0.3	0.3	0.28	
	loss angle	Φ	-	-	1×10^{-3}		3×10^{-4}	1×10^{-3}	1×10^{-4}	
	length	L	m	-	1.3	0.56	0.56	0.56	0.56	0.56
	diameter	d		-	2.1 2.3	1.6 1.8	0.3 0.4	0.85 1.2	0.6 0.6	0.20 0.25
	x-position	Dx		-	-	-	-	-	10	5
	z-position	Dz	mm	-	-	-	-	-	145 210	125 185
	radial distance to y-axis	Dr		-	-	-	150	-	-	-
	upper clamp y-position	Dyu		-	-5	-5	0	-5	0	0
	lower clamp y-position	Dyl		-	5	5	0	-2	0	0
GAS	resonant frequency	fGAS	mHz	60	250	250	-	-	-	-
	quality factor	QGAS	-	3	6	6	-	-	-	-
	saturation level	BGAS	dB	-60	-60	-60	-	-	-	-
IP	radial distance to y-axis	RIP	mm	600	-	-	-	-	-	-
	horizontal mode frequency	fIP	mHz	30	-	-	-	-	-	-
	quality factor	QIP	-	3	-	-	-	-	-	-
	saturation level	BIP	dB	-70	-	-	-	-	-	-

Figure 5.5: The parameters about the type-B vibration isolation systems. The upper values on the same column are the parameters for the recycling mirror syspension, while the lower values (written in red) are for the beam splitter suspension.

Modeling of heat links

The cryogenic suspensions and the radiation shield of the cryostat will be connected by seven pure aluminum wires with 1 mm thickness. The wires will be bent in a half circle shape with about 25 cm radius of curvature. As the seismic vibration is transmitted to the suspension system through the heat link wires, it is important to know their mechanical responses. The finite element analysis of the heat link wires has been performed by Y. Aso [57], and he calculated their mechanical frequency response. Figure 5.6 shows the geometry of the model structure used in his simulation, and Figure 5.7 shows the calculated frequency response. The solid lines show the calculated results from the finite element analysis, and the dashed lines show the transfer functions used in my simulation. In my model, the heat links are assumed to be a linear spring with different spring constants for the x, y and z directions, and its attenuation performance saturates at 10^{-4}-10^{-5} due to the mass distribution of the spring.
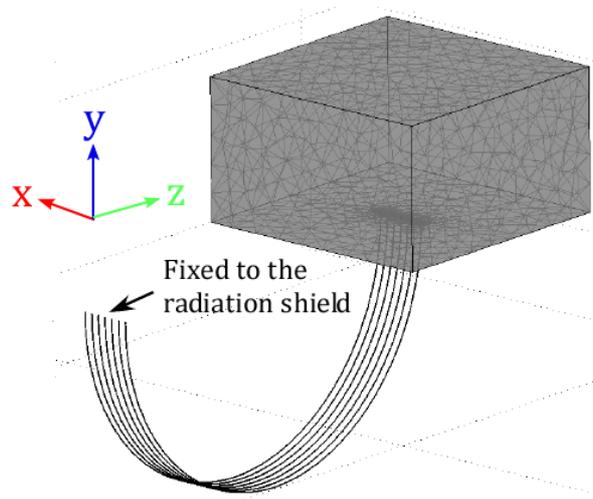
Figure 5.6: The model structure for the finite element analysis of the heat links [57].

Seismic Motion in Kamioka

The amplitude of the seismic motion displacement in the Kamioka mine was measured with the CMG-3T seismometer [1] in 2007 by A. Araya *et al.* Figure 5.8 shows the measured power spectrum of the ground displacement and its RMS amplitude on diffrent days. The blue and black solid lines show the measured spectra on a stormy day and a clear day respectively. In general, on a stormy day, the oceanic wave activity is increased and therefore the microseismic peak around 100-300 mHz is enhanced. The RMS displacement in the Kamioka mine is normally ~ 0.1 μm at 0.1 Hz, while it is enhanced to ~ 1 μm on stormy days. As a gravitational wave detector must be operated continuously over a span of $\sim$years, the vibration isolation systems have to be designed so that it can be operated stably even on stormy days. Therefore, the "noisy" spectrum in Figure 5.8 will be used in the following simulation.

---

[1]Güralp Systems Ltd. (U.K.) `http://www.guralp.com/`
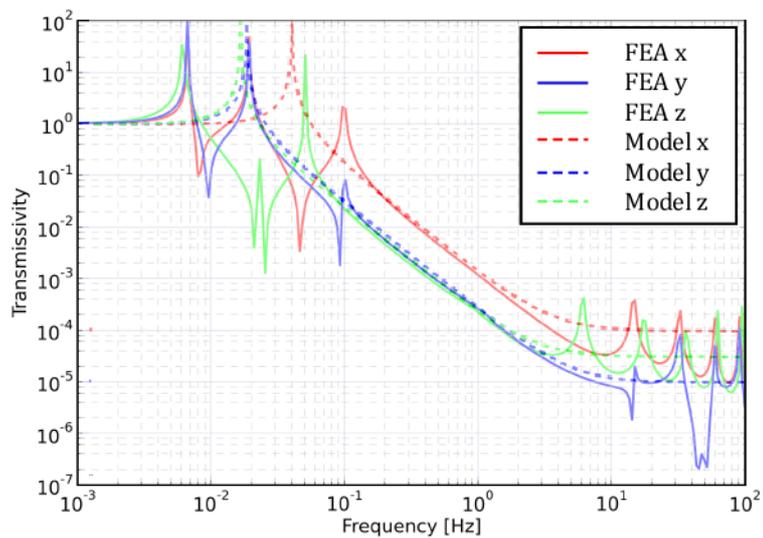
Figure 5.7: Transfer functions of the heat links. The solid lines show the calculated results from the finite element analysis and the dashed lines show the transfer functions assumed in my simulation.
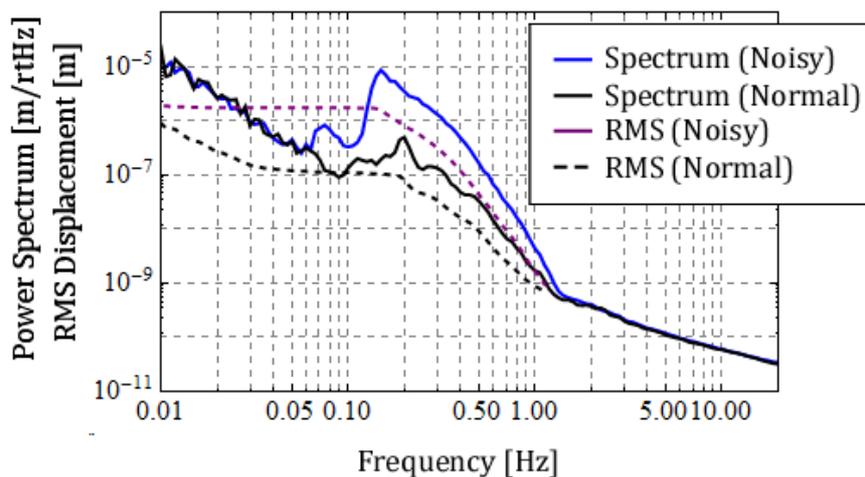
Figure 5.8: Measured seismic spectrum and RMS displacement in the Kamioka mine.

5.2 Translational Modes

5.2.1 Seismic Attenuation Performance of the Type-A System

Figure 5.9 shows the calculated transfer function from the horizontal seismic motion to the longitudinal displacement of the test mass. In the type A system, seismic vibration is transmitted to the mirror motion through two paths. The first path is the one through the suspension chain from the upper floor of the tunnel, and the second path is the one through the heat links from the cryostat. The cyan solid line in Figure 5.9 shows the transmissivity of the vibration through the first path and the green solid line shows that through the second path. The red dashed line represents the sum of the two transmissivity. From the plot, one can see that the induced vibration through the first path is significant at low frequencies (< 1 Hz) and therefore determine the RMS amplitude of the mirror displacement. The vibration through the second path is siginificant at high frequencies (> 1 Hz) and therefore it can possibly affect the sensitivity of the interferometer.
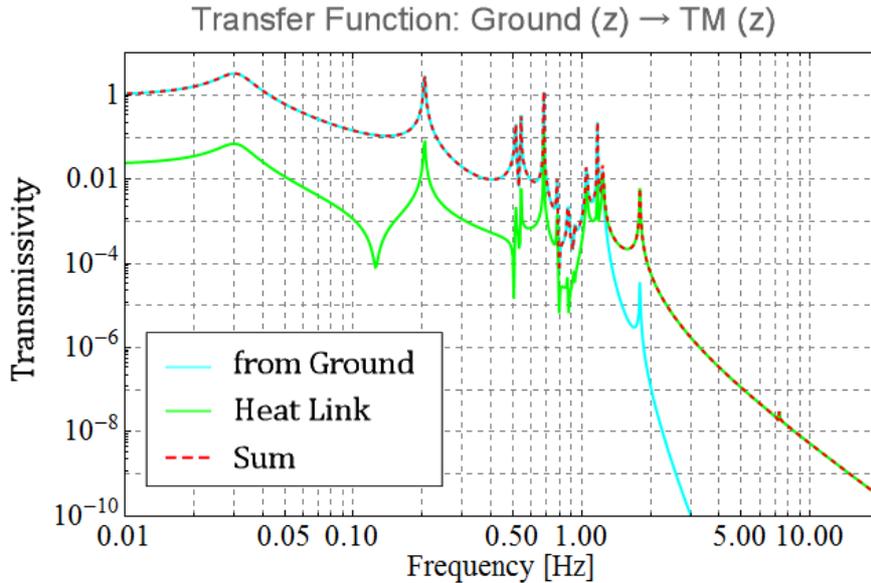
Figure 5.9: Transfer function from the seismic motion to the mirror motion (in z-direction) of type-A system through the two different paths.

Figure 5.10 shows the transfer function from the vertical seismic motion to the vertical displacement of the test mass. Alike the horizontal vibration, the vertical vibration through the heat links is dominant at high frequencies (> 1 Hz). The difference from the horizontal mode is the existence of the resonant peaks at high frequencies. The resonant peaks at 20-30 Hz are due to the bounce modes of the suspension wires for IR and RM, and the peak around 100 Hz is due to the bounce of the sapphire fibers suspending TM.

Figure 5.11 shows the expected power spectrum of the test mass displacement induced by the seismic vibration. In the calculation, it is assumed that the cryostat is vibrating at the same amplitude as the ground. Taking into account the vertical-longitudinal coupling of 0.3% by the tilt of the interferometer, the mirror fluctuation induced by the seismic vibration is dominated by the couplings from the vertical noise above 20 Hz. Note that
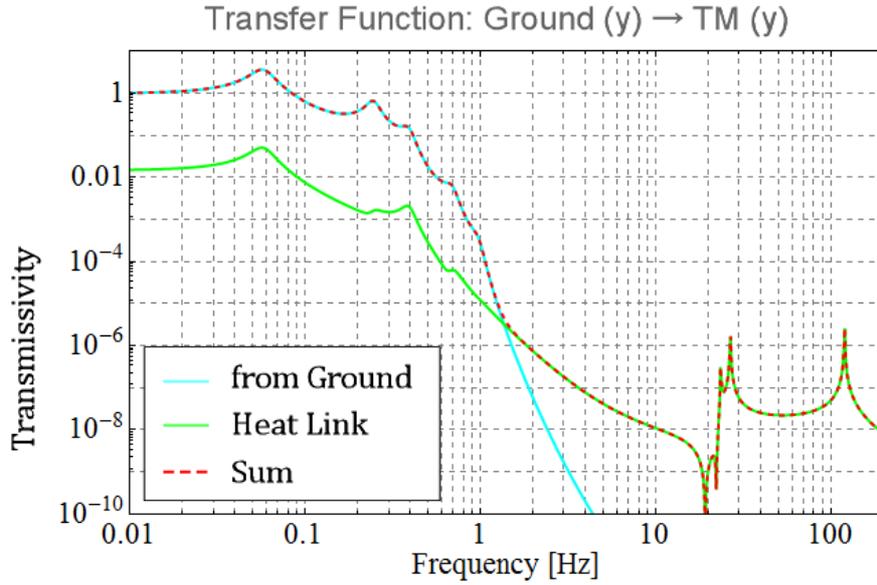
Figure 5.10: Transfer function from the seismic motion to the mirror motion (in y-direction) of type-A system.

this estimation includes the seismic noise only, not the leakage of vertical thermal noise into the horizontal one, which should be estimated separately. Figure 5.12 shows the high frequency part of Figure 5.11. The purple line shows the corresponding test mass displacement to the target sensitivity of LCGT.

5.2.2   Design Consideration on the Type-A System

Although the estimated residual seismic noise level is lower the level of the target sensitivity above 10 Hz, it does not meet the requirement (3×10^{-20} m/$\sqrt{\text{Hz}}$ at 10 Hz) and there is a risk that the seismic noise may exceed the target noise level. The internal resonances of the mechanical filters or the violin modes of the wires would be excited by the seismic vibration and pollute the interferometer sensitivity. In addition, there is no assurance that the vibration of the cryostat is the same as the ground vibration. Actually, in CLIO (Cryogenic Laser Interferometer Observatory, which is the prototype of LCGT that was built in the Kamioka mine), the vibration inside the cryostat has been observed to be 10-100 times larger than the ground vibration at the frequency between 10 and 100 Hz (Figure 5.13). If it is assumed that the cryostat in LCGT vibrates at the same level, the interferometer sensitivity would be degraded in the observation frequency band (> 10 Hz).

In order to attenuate the seismic noise introduced from the cryostat vibration through the heat links, two solutions are suggested:

1. The heat links are attached not to the platform (PF) but to the intermediate recoil mass (IR) to insert one more cushion between the heat links and the test mass (Figure 5.14 left).

2. Another mechanical filter is introduced inside the cryostat and the vibration of the heat links is passively attenuated (Figure 5.14 right).
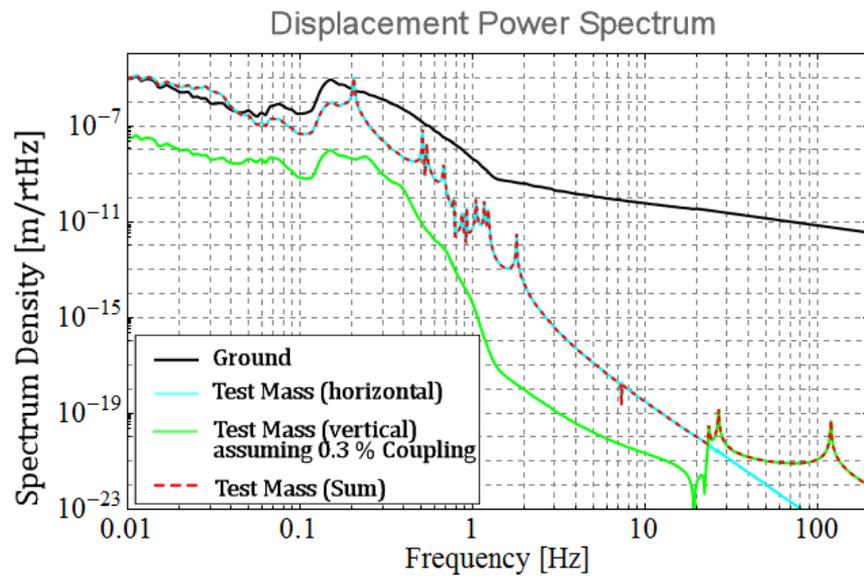
Figure 5.11: Estimation of the test mass displacement induced by seismic vibration.
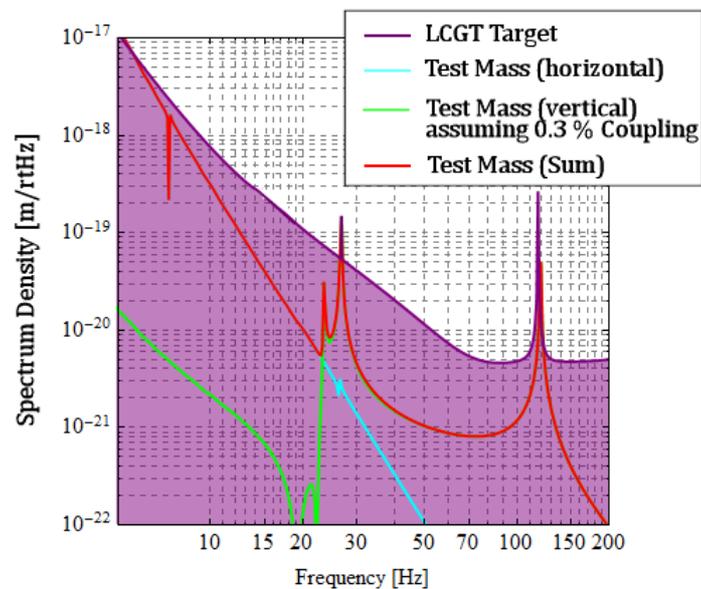
Figure 5.12: The high frequency part of Figure 5.11 and comparsion with the corresponding test mass displacement to the LCGT target sensitivity.
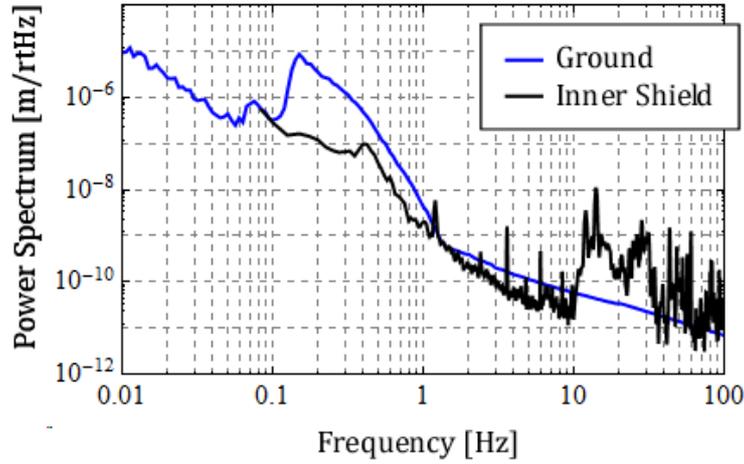
Figure 5.13: The comparison of the vibration on the ground and inside the cryostat. The vibration inside the cryostat were measured by K. Yamamoto with the handmade interferometric seismometer [58].
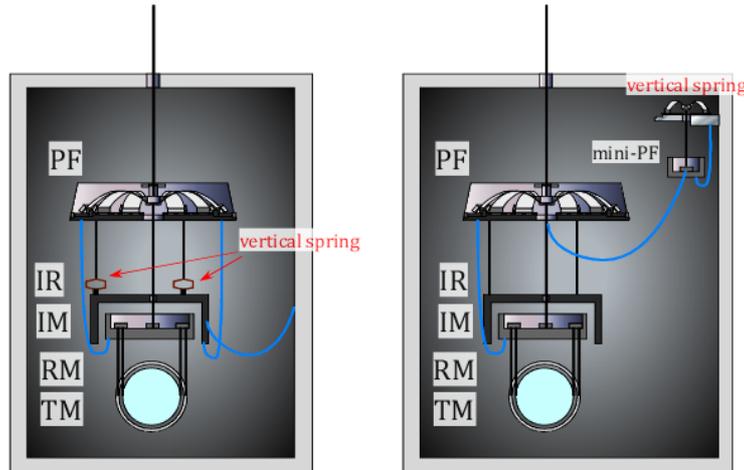

Figure 5.14: Two kinds of design arrangement to improve the attenuation performance.

The first suggestion is attaching the heat links to IR. In order to attenuate the vertical vibration, small vertical springs with resonant frequencies of ~ 5 Hz are introduced to the IR suspension (Figure 5.14 left). The red solid line in Figure 5.15 shows the spectrum density of the test mass displacement when the heat links are attached to IR and the vertical springs are introduced to the IR suspension. Compared with the conventional plot (the red dashed line in Figure 5.15), the attenuation performance is improved by 2-3 orders of magnitude above 10 Hz by this design arrangement.

The second way to improve the seismic attenuation is introducing an additional mechanical filter to pre-isolate the cryostat vibration. The stage for the heat link pre-isolation is suspended by a single wire and a vertical spring to achieve seismic attenuation in all six DoFs (Figure 5.14 right). The heat links are attached to the cryogenic suspensions via this stage. When the resonant frequenies of the mechanical filter are tuned at ~ 1 Hz both in
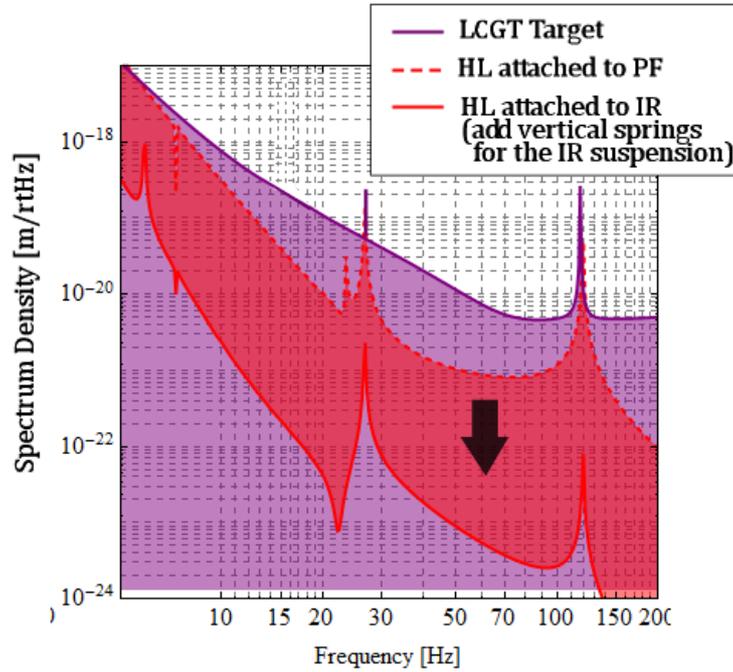
Figure 5.15: Improvement of the attenuation performance by the design arrangements.

the horizontal and the vertical directions, the seismic noise would be suppressed by 2 orders of magnitude at 10 Hz and more at higher frequencies. The attenuation performance can be boosted by cascading attenuation stages. However, in this method, as the amount of mass inside the cryostat is increased, the initial cooling time of the syspension system would be increased.

5.2.3   RMS Displacement of the Test Mass

Figure 5.16 shows the low frequency part of Figure 5.11 and the RMS amplitude of the ground and the test mass displacements. The main contributor to the RMS displacement of the mirror is the resonant peak at 0.2 Hz, overlapping with the microseismic peak. This peak corresponds to the pendulum mode of the attenuation chain where all the suspended masses move in the common direction. Its mode shape is drawn in the right of Figure 5.16. It is difficult to shift the resonace away from the microseismic peak, because its resonant frequency is determined mainly from the total length ($\sim$ 13 m) of the attenuation chain, which has been fixed from the tunnel design and minimum rock thickness considerations. One needs to critically damp the resonance at 0.2 Hz to suppress the RMS displacement of the mirror. The damping would be achieved by the active controls using sensors and actuators on the pre-isolator. If the peak is critically damped, the RMS amplitudes of the test mass displacement and velocity are improved to $\sim$ 0.1 μm and $\sim$ 0.1 μm/s.
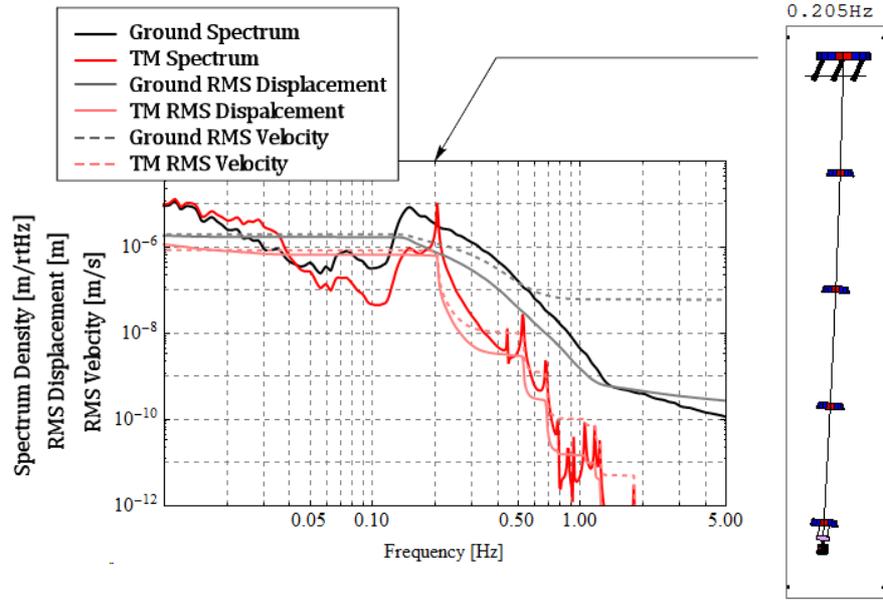
Figure 5.16: The power spectrum and RMS amplitude of the ground and the test mass displacement, and their RMS velocity after the contribution of the IP is taken into account.

5.2.4   Performance of the Type-B System

The calculated transfer functions from the ground horizontal displacement to the mirror longitudinal displacement of type-B systems are plotted in Figure 5.17. The cyan line represents the transfer function of the recycling mirror suspension and the pink line represents that of the beam splitter suspension. In both cases, the transfer functions drop rapidly above 2 Hz, resulting in attenuation factors of $\sim 10^{-12}$ at 10 Hz. On the other hand, the calculated transfer functions from the ground vertical displacement to the mirror vertical displacement are shown in Figure 5.18. The transfer functions drop rapidly above 0.5 Hz, while their slope getting shallower because of the CoP effect in the GAS filters. Above 10 Hz, the attenuation performance is degraded by the resonant peaks of the vertical bounce modes of the suspension wires.

Figure 5.19 shows the the power spectrum of the mirror longitudinal displacement induced by the seismic vibration. Taking into account the vertical-longitudinal coupling of 0.3%, the mirror fluctuation is dominated by the couplings from the vertical noise above 5 Hz. The dashed lines in Figure 5.19 represent the requirements on the displacement of the beam splitter and the recycling mirror, which are discussed in chapter 3. One can see that the expected mirror displacements are well below the required levels.

Figure 5.20 shows the low frequency part of Figure 5.19 and the RMS amplitude of the ground and the recycling mirror displacements. Since the resonant peaks are absent at the microsesmic peak (100-300 mHz), the expected RMS displacement and velocity of the mirror are smaller than those of the test mass.
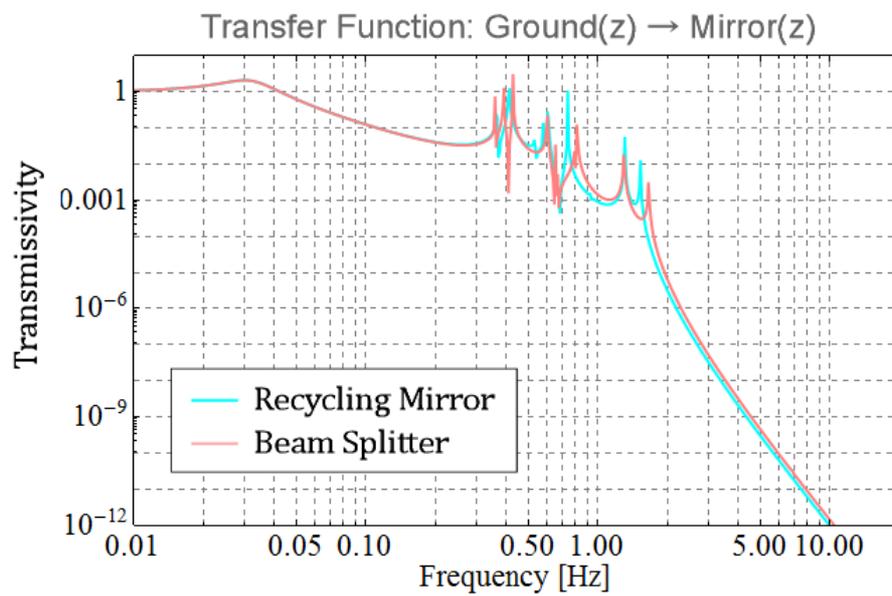
Figure 5.17: Transfer functions from the ground displacement to the mirror displacement of the type-B system, in the horizontal direction.
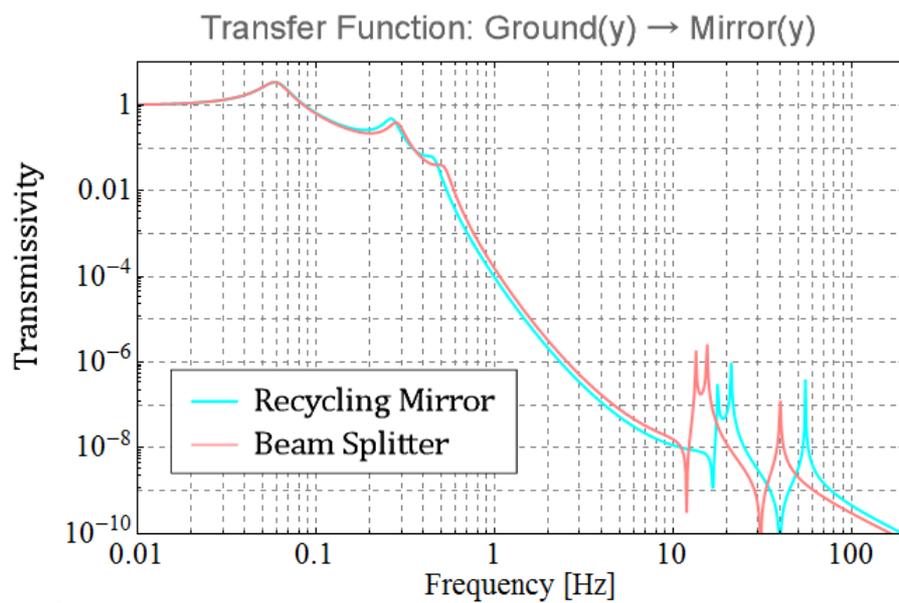
Figure 5.18: Transfer functions from the ground displacement to the mirror displacement of the type-B system, in the vertical direction.
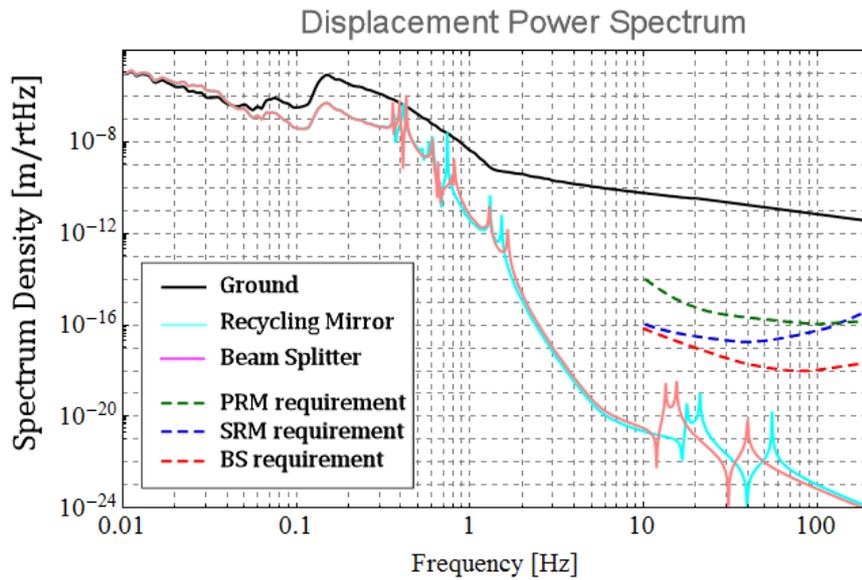
Figure 5.19: Estimation of the mirror displacement induced by seismic vibration in the type-B system.
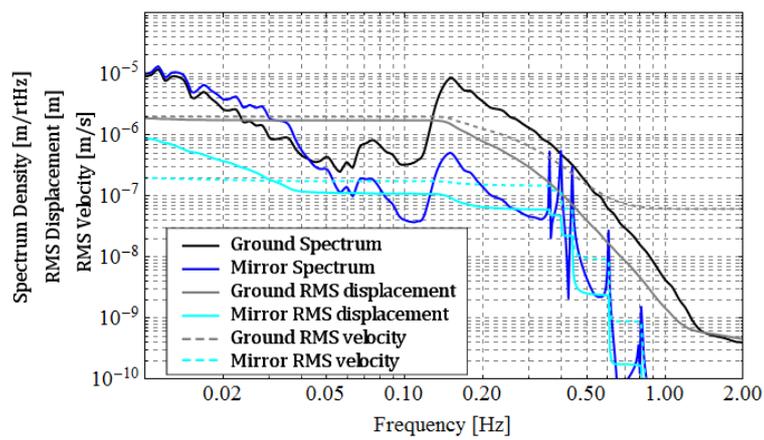

Figure 5.20: The power spectrum density and RMS amplitude of the ground and the recycling mirror displacement.

5.3 Rotational Modes

5.3.1 Rotational Motions and Asymmetries

As mentioned in chapter 4, the rotational motions of an object tend to be excited by the couplings from the translation motions due to mechanical imperfections and misalignments. Therefore, in order to estimate the mirror angular displacements, one needs to introduce some asymmetries to the vibration isolation systems. The asymmetries which can be introduced to the vibration isolation systems are :

- Asymmetry in the effective spring constants of the IPs

- Deviation of the wire clamping points from the ideal position

- Asymmetry in the wire thickness and length of the mirror suspensions

- Deviation of the attachment point of the heat links from the gravity center

Without any asymmetry in the system, the yaw motion of an object never couples to the motions of other DoFs, while the pitch motion couples to the longitudinal motion through the mismatch of the suspension point and its center of mass (Figure 5.21). Figure 5.22 shows the power spectrum and RMS amplitude of the test mass pitch motion induced by the couplings from the longitudinal seismic noise. It is assumed that the heat link is attached to PF and the radiation shield of the cryostat is vibrating at the same amplitude as the ground. The RMS amplitude of the mirror pitch motion is $\sim 0.1 \ \mu$m in this case.
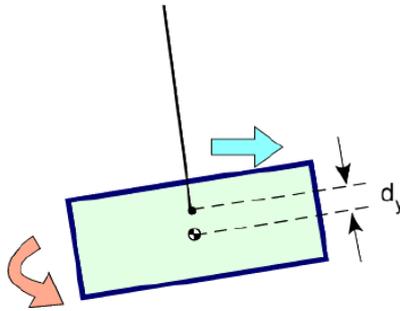
Figure 5.21: Tilt-translation coupling.

When the asymmetries are introduced to the system, the yaw motions of the objects are excited by the translation-yaw couplings, and the pitch motions are enhanced by the increased cross-couplings.

5.3.2 Test Mass Angular Displacement

Since it is impossible to expect the asymmetries in the actual systems, the mirror angular displacements are estimated by the use of Monte-Carlo methods, i.e. the asymmetries are randomly introduced to the system and the computation is iterated for many times. The asymmetries assumed in the simulation are summerized in Table 5.1.
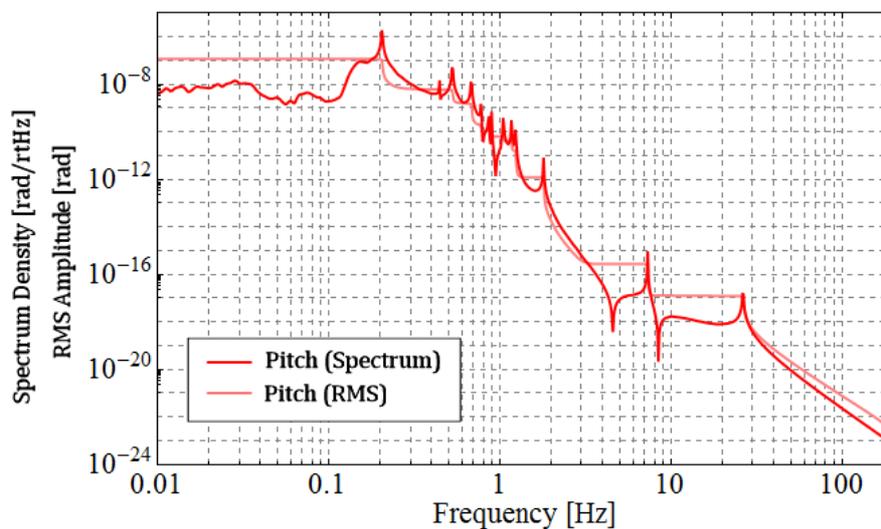
Figure 5.22: Power spectrum and RMS amplitude of the test mass pitch motion.

Parameter	Value
Effective spring constant of IP	$\pm50\%$
Wire clamping position	±0.5 mm for each direction
Wire diameter	±5 %
Wire length	±0.5 mm
Attachment point of the heat links	±5 cm for each direction

Table 5.1: Asymmetries assumed in the simulation.

In my simulation, the heat links are assumed to be a linear spring connecting the radiation shield of the cryostat and one point of the attached mass. In the simulation described above, it was implicitly assumed that the spirng is attached to the gravity center of the attached mass. When the attachment point of the spring is not coincident with the gravity center, the translational motions couple to the rotational motions of the attached mass.

Figure 5.23 shows the calculated angular displacement of the test mass induced by the seismic vibration. In the simulation, the physical and geometric parameters are arranged randomly in the ranges of Table 5.1, and the calculation is repeated by 20 times. The area filled in red or blue shows the fluctuation range of the calculated mirror pitch/yaw displacement over the iteration. It is assumed that the radiation shield of the cryostat is vibrating at the same level as the ground. Note that the model includes the eddy current damper at the top of the chain, therefore the resonant peaks of the yaw modes at 10-100 mHz are efficiently damped. The eddy current damping adopted to the attenuation chain will be detailed in chapter 6.
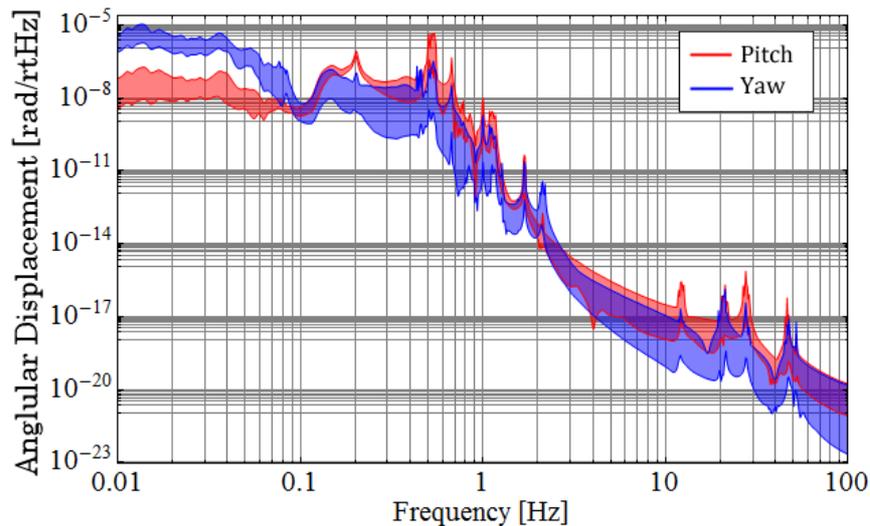
Figure 5.23: Power spectrum of the test mass pitch and yaw displacement.

Figure 5.24 and 5.25 show the contribution of each kind of asymmetry to the mirror angular motions. From Figure 5.24, one can see that the mirror pitch motion is not largely affected by the asymmetries. and thus it mainly comes from the longitudinal-pitch couplings due to the mismatches of the suspension points and the center of mass positions. On the other hand, the mirror yaw motion is largely affected by the asymmetries. At low frequencies (< 0.1 Hz), the main contributors to the yaw motion are the asymmetry in the IP stiffness and the deviation of the attachment point of the heat link wires, and at high frequencies, the yaw motion is mainly excited by the deviation of the wire suspension points.

Figure 5.26 shows the optical path changes due to the mirror angular fluctuation, assuming that the beam spot is off-centered by 1 mm. The black line shows the translational displacement of the mirror, assuming a 1% coupling from the vertical noise. In these assumptions, the impact on the sensitivity by the angular motion is smaller than the impact
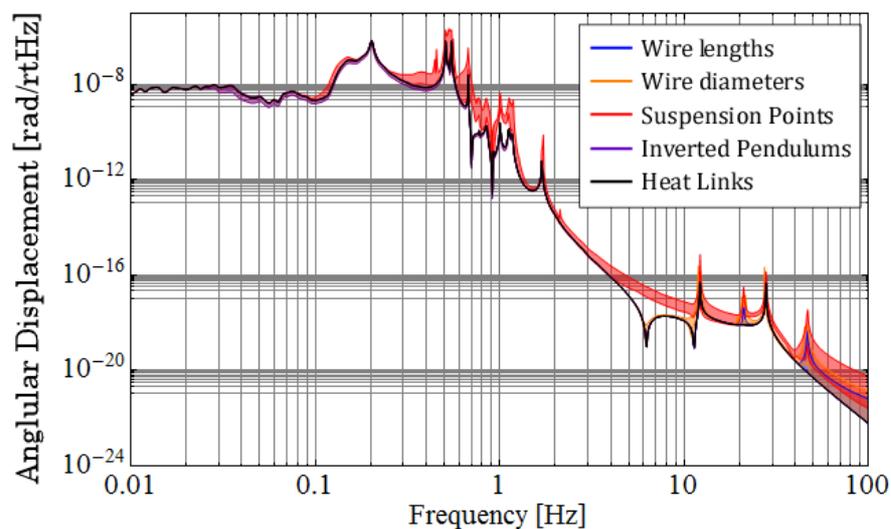
Figure 5.24: Contribution of each kind of asymmetry to the mirror angular displacement (in the pitch mode).
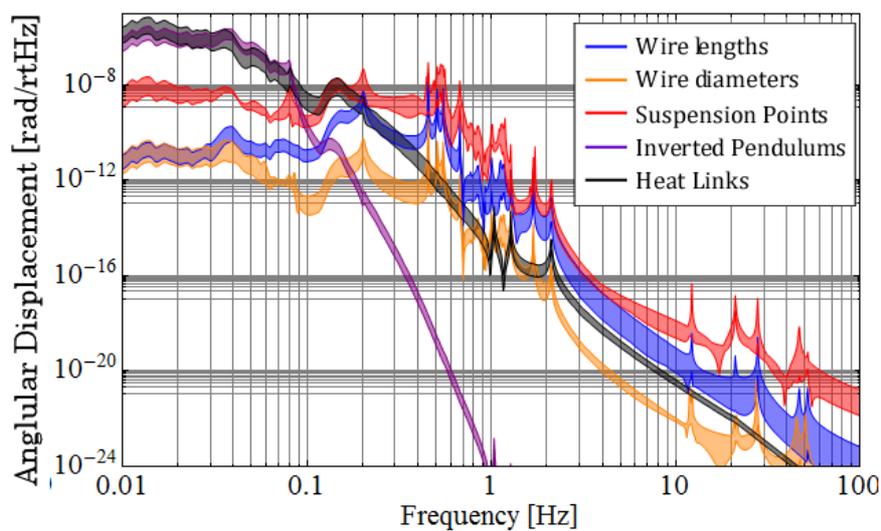

Figure 5.25: Contribution of each kind of asymmetry to the mirror angular displacement (in the yaw mode).

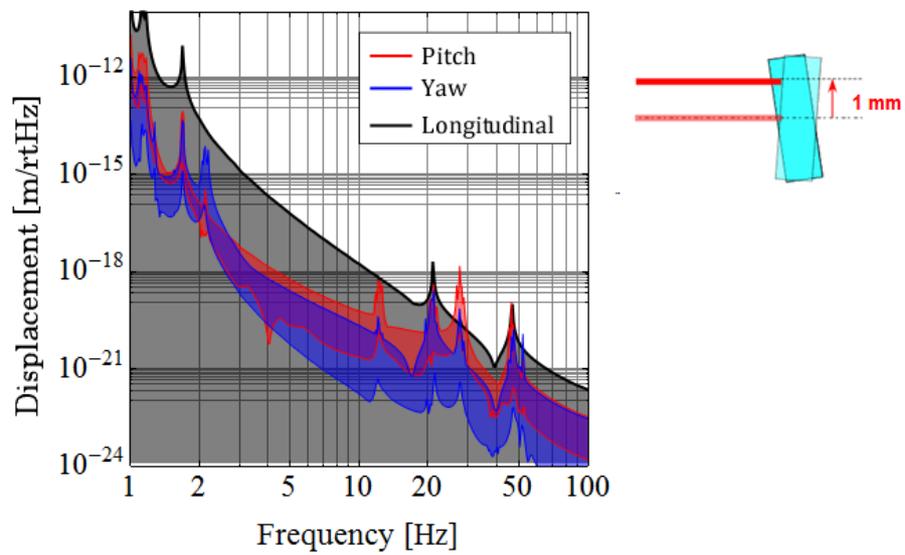by the translational motion, except at the resonant peak at ~ 30 Hz.

Figure 5.26: Impact on the sensitivity of the interferometer by the mirror angular fluctuation.

Chapter 6

Torsion Mode Damping

6.1 Overview

In order to attenuate the vertical seismic motions of the mirrors, cascades of GAS filters are employed on the vibration isolation systems of LCGT. Each GAS filter is suspended by a single wire, to achieve seismic attenuation in the three rotational DoFs. Due to the softness of the wire in its torsional movement and the large moment of inertia of the filter around the vertical axis, the yaw modes of the attenuation chain have quite low (in the order of 10 mHz) resonant frequencies, and therefore the yaw motions of the filters are isolated well.

However, since these modes have long decay time due to their high quality factors ($\gtrsim 100$), the filters will keep oscillating once these modes are excited. It was observes that the oscillation amplitude of the mirror rotation angle grows easily to levels of milli-radians by the actions of earthquakes or the accidentally wrong controlling forces. This large mirror motion utterly exceeds the range of the mirror actuators and thus disturbs the interferometer operation for a long time. In TAMA-SAS, which also utilizes single-wire suspensions, it took several hours to resume the interferometer lock, without any damping mechanism for the torsion modes. During this time we cannot run the observation of gravitational waves, and thus the duty time of the detector decreases. The damping mechanism for the torsion modes is indispensable for the continuous observation of gravitational waves.

In TAMA, the yaw modes are damped by active damping system, which utilizes photo sensors to measure the rotation angle of the intermediate stage, and feeds their signals back to the actuators on the top of the attenuation chain (Figure 6.1). By introducing this damping system, the quality factors of the torsion modes are reduced to less than 10 [59]. However, due to the limited dynamic range of the photo sensors, the system still stops operation for large excursion of the rotation angle.

In LCGT, the torsion modes of the attenuation chain will be damped passively by eddy current dampers, to avoid the above-mentioned dynamic range problems of the sensors and actuators. Figure 6.2 shows the conceptual design of the damping system. A disc with a number of permanent magnets is suspended from the top filter and produces braking torques between the damper and a conductive plate attached on the filter 1. The yaw motions of the lower stages are also damped, if one chooses the torsional stiffness of the
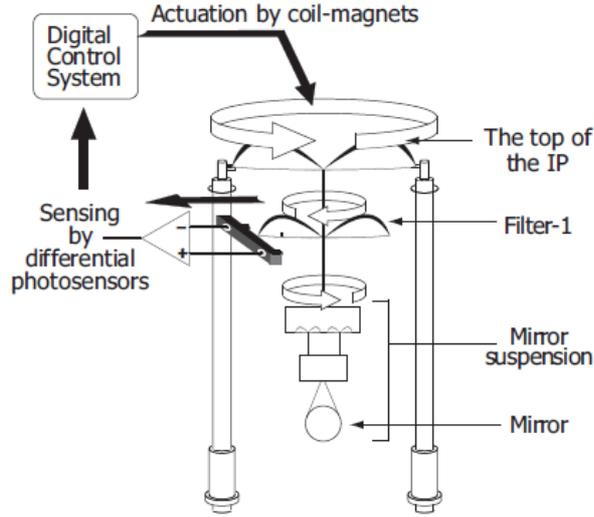
Figure 6.1: Conceptual diagram of the torsion mode control system in TAMA-SAS [59].

wires properly. The optimization of the torsional stiffness and the damping strengh will be performed in the following sections.

Since the magnetic damper damps the motions of the filters in other DoFs as well, it may also work as a damper for the pendulum modes and vertical modes of the chain. As described in section 2.4, a rigidly-held viscous damper may degrade the attenuation performance at high frequencies, therefore the damper is suspended by three wires and thus held flexibly in the horizontal directions. The effect of the damper on the pendulum modes and vertical modes of the chain will be discussed in the latter part of this chapter.

6.2 Models and Parameters

In order to investigate optimal parameters for the torsion mode damping, simple one-dimensional models about the yaw modes of the attenuation chains are constructed. Figure 6.3 shows the schematic view of the model structure about the type-A and the type-B system. In this model, the system is assumed to be a three/five stages torsion pendulum with viscous damping between the first stage and the magnetic damper which is fixed to the ground. For simplicity, I assume the inverted pendulums and the multi-wire suspensions as rigid structures, since they have much higher resonant frequencies than the single-wire suspensions in yaw modes. Therefore, the intermediate mass, the recoil mass and the mirror are assumed to be one unit in the model.

The parameters used in the simulation are summerized in Table 6.1. The moment of inertia around the vertical axis of each stage is calculated from the parameter list in Figure 5.2. The minimum wire diameters are chosen so that the tensile stress of every wire does not exceed 800 N/mm². The yield tensile strength of maraging steel is ~ 1800 N/mm² and that of bolfur is ~ 3400 N/mm², therefore they have safety factors of more than 2. The torsional stiffness of the wire is calculated from the shear modulus and the wire diameter by eq. (4.5).
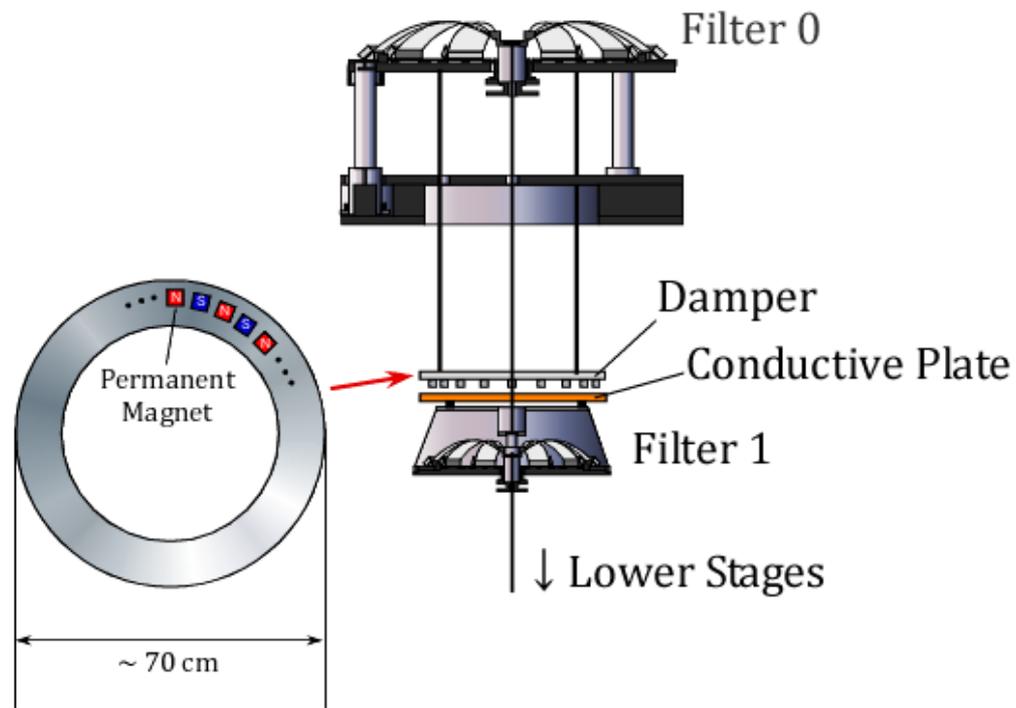
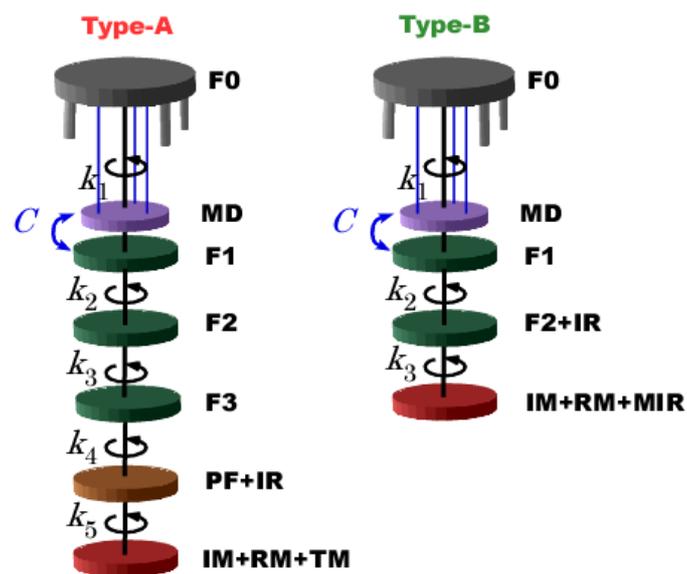Figure 6.2: Conceptual desing of the damping system for the torsion modes.

Figure 6.3: Schematic view of the yaw mode model structure of the type-A and type-B system.

	I_y [kg m^2]	Material	G [GPa]	$d_{\rm w}$ [mm]	L [m]	$k_{\rm t}$ [Nm/rad]
F1	6.4	maraging	75	> 3.1	3.05	> 0.22
F2	6.4	maraging	75	> 2.8	3.05	> 0.15
F3	6.4	maraging	75	> 2.5	3.05	> 0.094
PF+IR	8.8	bolfur	60	> 2.2	3.05	> 0.046
IM+RM+TM	0.89	maraging	75	> 1.3	0.40	> 0.12

Table 6.1: The parameters used in the simulation for the type-A system. I_y, G, $d_{\rm w}$ and $k_{\rm t}$ represent the moment of inertia around the vertical axis, the shear modulus of the wire material, the wire diameter and the torsional stiffness.

6.3   Parameter Optimization

To estimate the decay time of the torsional modes, the transfer function from the external torque acting on the TM to the angular displacement of the TM is calculated. Figure 6.4 shows the calculated transfer function with various damping strength [Nm/(rad/s)] of the damper. The wire diameters are chosen the minimum values shown in Table 6.1. Using these parameters, we note that the torsion mode at 50 mHz is not damped by the magnetic damper, because in this mode only the last stage rotates and the it never couples with the rotation at the top of the stage.
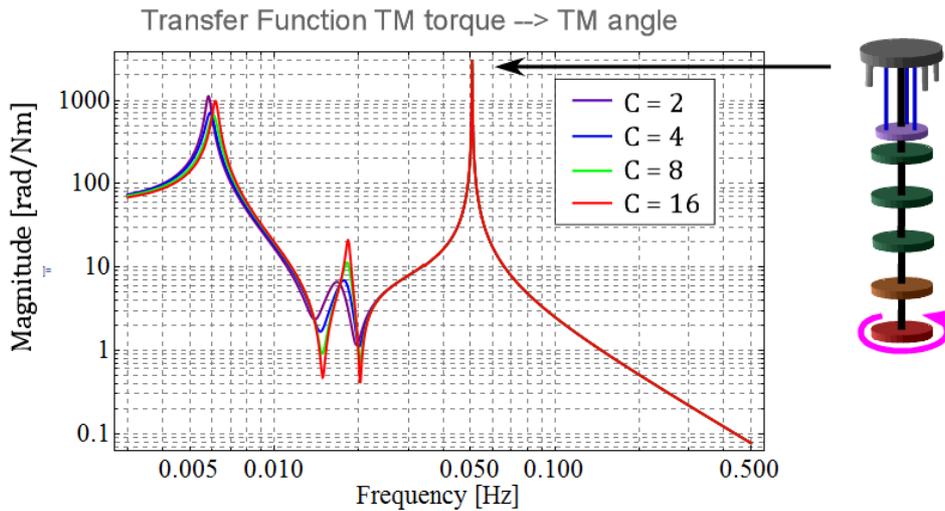
Figure 6.4: Transfer function from the external torque on the TM to the angular displacement of the TM with minimum wire diameters.

Looking at the parameters in Table 6.1, the last stage has relatively small moment of inertia, and thus has to be suspended by a soft wire to make its motion well coupled with the motion of the upper stages. The wires suspending F3 and PF are too soft in the torsion modes with the minimum diameters, so that one needs to make them thicker to balance the stiffness of the whole chain. Table 6.2 shows the parameters newly proposed for the torsion mode damping. The top wire is designed to be softer than the wires for the lower suspensions, so that the lowest resonant mode is effectively damped.

	d_{w} [mm]	L [m]	k_{t} [Nm/rad]
F1	3.1	3.05	0.22
F2	3.8	3.05	0.50
F3	3.8	3.05	0.50
PF+IR	4.0	3.05	0.50
IM+RM+TM	1.6	0.40	0.12

Table 6.2: The wire parameters newly proposed for the torsion mode damping.

Although the torsional stiffness of the wires can be increased by thickening them, wires with large thickness may possibly degrade the horizontal attenuation performance of the vibration isolation systems due to their bending elasticity (as discussed in section 4.3). The bending elasticity of a wire only depends on the wire thickness in the first few cm from the suspension points, while the torsional stiffness depends on the thickness integrated over the wire length. Therefore, we design wires with large thickness in the middle and small thickness at the both ends as shown in Figure 6.5, to obtain large torsional stiffness without increasing the bending elasticity. The diameters shown in Table 6.2 represent the thickness in the middle of the wires.
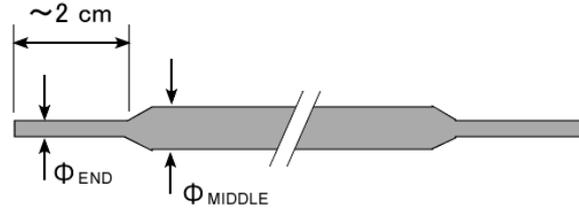
Figure 6.5: Schematic design of the wire for the attenuation chain.

Figure 6.6 shows the calculated transfer function with various damping factors and the new parameters. The lowest resonant mode is almost critically damped and the other modes are also damped well ($Q < 10$). The impulse response of the system, in Figure 6.7, demonstrates that the torsional motions are damped with the decay time of ~ 1 minute.

Robustness Check

As the torsional stiffness is proportional to the forth power of the wire diameter, the actual stiffness may vary from the ideal value due to the machining accuracy problem, and the individual difference of the shear modulus. To check how robust the damping system is to such deviation, I arrange the wire diameter randomly in the range of $\pm 5\%$ and check the heights of the resonant peaks. Figure 6.8 shows the superimposed plots of the calculated transfer functions over 100 iterations. One cannot see any resonant peaks as high as $Q = 10$, thence the damping system is robust with respect to the wire diameter variance.
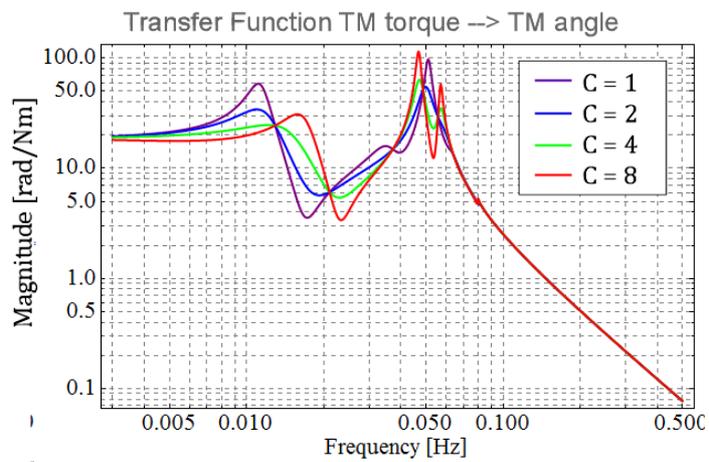
Figure 6.6: Transfer function from the external torque on TM to the angular displacement of TM with new parameters.
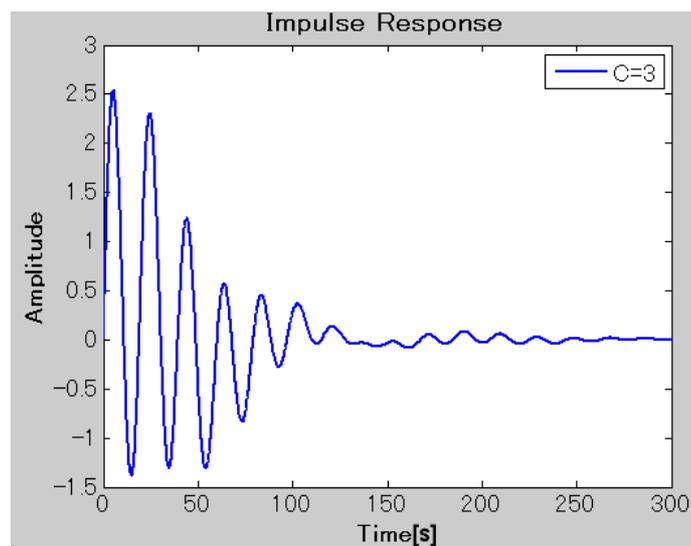

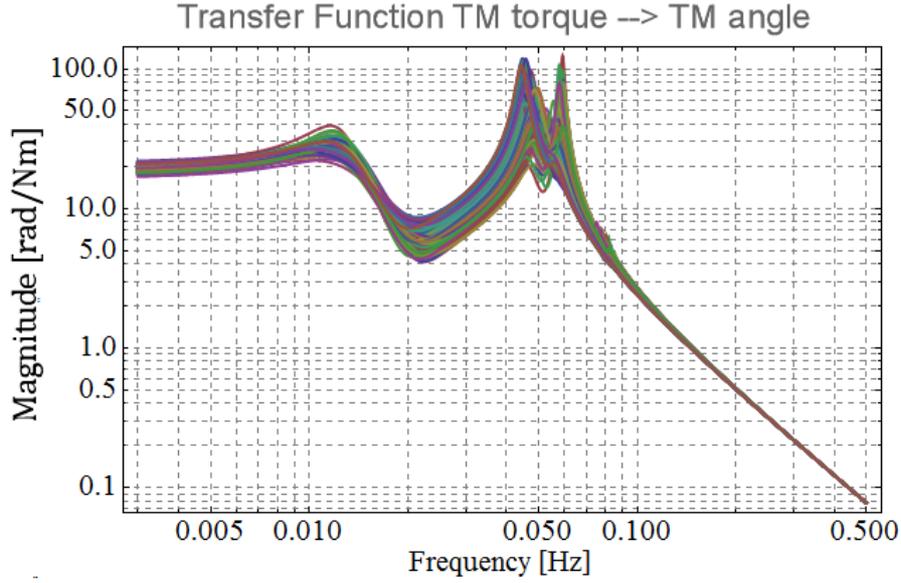Figure 6.7: Impulse response to the external torque.

Figure 6.8: Transfer function with $\pm 5\%$ deviation of the wire thickness.

6.4 Damping for Type-B System

The parameters for the torsion mode damping of the type-B systems are summarized in Table 6.3. The calculated transfer functions and the impulse responses are plotted in Figure 6.9 and 6.10. In both cases, the torsional modes will be damped with the dacay time of 1-2 minutes.

	I_y [kg m^2]	Material	G [GPa]	d_{w} [mm]	L [m]	k_{t} [Nm/rad]
F1	6.4	maraging	75	2.3	1.30	0.16
F2+IR	6.8 (8.1)	maraging	75	2.3	0.56	0.32
IM+RM+TM	0.42 (1.3)	maraging	75	1.2	0.56	0.024

Table 6.3: The parameters used in the simulation for the type-B system. The values in the bracket is for the beam splitter suspensions.

6.5 Damping Effect on Other DoFs

The magnetic damper damps the motions of the lower stages in other DoFs as well. Considering a magnets moving above the conductive surface, the braking force is applied both for the movement in the parallel and the perpendicular directions to the surface. If the conductive surface is a simple plane, the damping factor for the perpendicular movement is several times larger than that for the parallel movement, because the gradient of the magnetic field is larger in the perpendicular direction. To estimate the effect of the damper for other DoFs, I assume that the damping factor for the perpendicular movement is 2.5 times larger than that for the parallel movement [32].

For simplicity, the magnetic damper is assumed to be a ring of 30 cm radius, having the uniform damping strength (per unit length) all along the ring. From the required damping
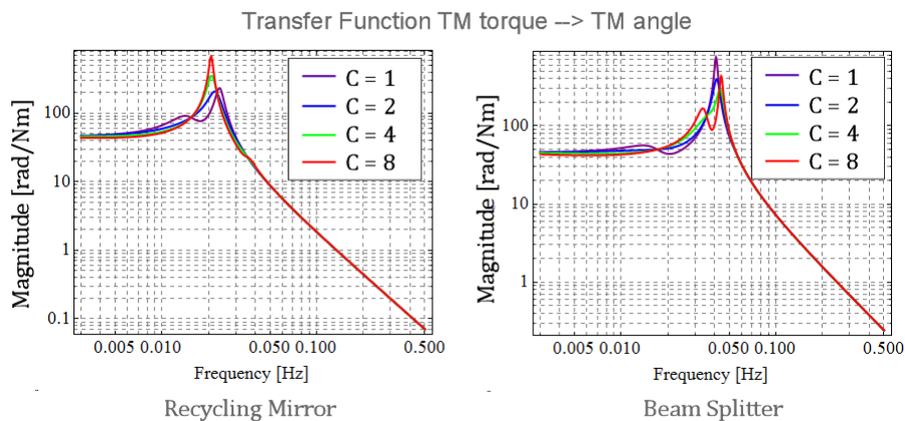
Figure 6.9: Transfer function from the external torque on the mirror to the angular displacement of the mirror.
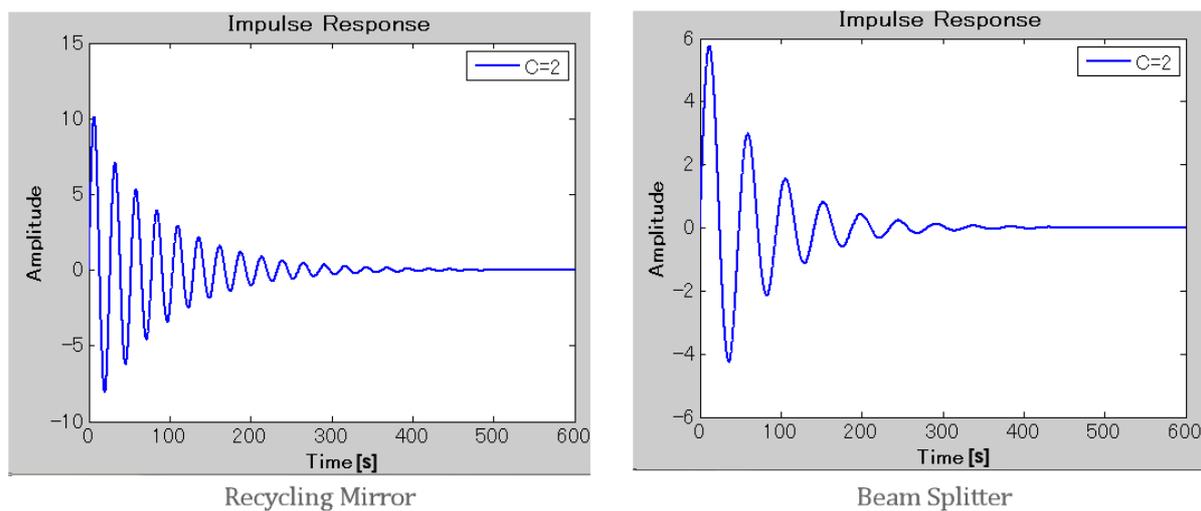

Figure 6.10: Impulse response to the external torque.

strength for the torsion mode ~ 4 N m/(rad/s) in the type-A system, the damping strength for the other DoFs are estimated as in Table 6.4. The damping strengths in the type-B system are about the half of these values.

DoF	Damping factor	
x (horizontal)	36	
y (vertical)	90	kg/s
z (horizontal)	36	
pitch	5.0	
yaw	4.0	N m/(rad/s)
roll	5.0	

Table 6.4: The damping strength of the magnetic damper for each DoF.

Parameter	Value
mass	30 kg
moment of inertia (x)	1.3 kg/m^2
moment of inertia (y)	2.5 kg/m^2
moment of inertia (z)	1.3 kg/m^2
number of wires	3
wire diameter	0.3 mm
wire length (type-A)	2.81 m
wire length (type-B)	1.10 m
wire material	C-70 steel

Table 6.5: The parameters on the damper and its suspension.

From the calculated damping strengths, the damping effects on the pendulum modes and vertical modes of the attenuation chain are investigated. The parameters on the damper and its suspension are described in Table 6.5. Figure 6.11 shows the comparison of the longitudinal displacement of the test mass with and without the magnetic damper. The magnetic damper suppresses several resonant peaks by factors of 2-4. It is a welcome result that the resonant peak of the lowest pendulum mode at 0.2 Hz is damped by a factor of 3 and the RMS displacement of the mirror is suppressed. Nevertheless, to further suppress the RMS displacement of the test mass to the required level (0.1 μm), one needs to damp this mode almost critically and therefore additional damping with active control sytems would be required in any case.

Figure 6.12 shows the transfer function from the vertical ground displacement to the test mass displacement in the vertical direction. As the damper is rigidly supported in the vertical direction, the attenuation performace is degraded at high frequencies up to the vertical bounce mode of the damper suspension (~ 6 Hz). In the type-A system, however, the vertical vibration of the test mass at > 1 Hz is mostly contributed by the vibration transmitted through the heat links, thus the degradation due to the damper does not affect the sensitivity at those high frequencies.

Figure 6.13 shows the longitudinal displacement of the beam splitter with damper and without damper. In the calculation, 0.3% of the vertical-longitudinal coupling is taken
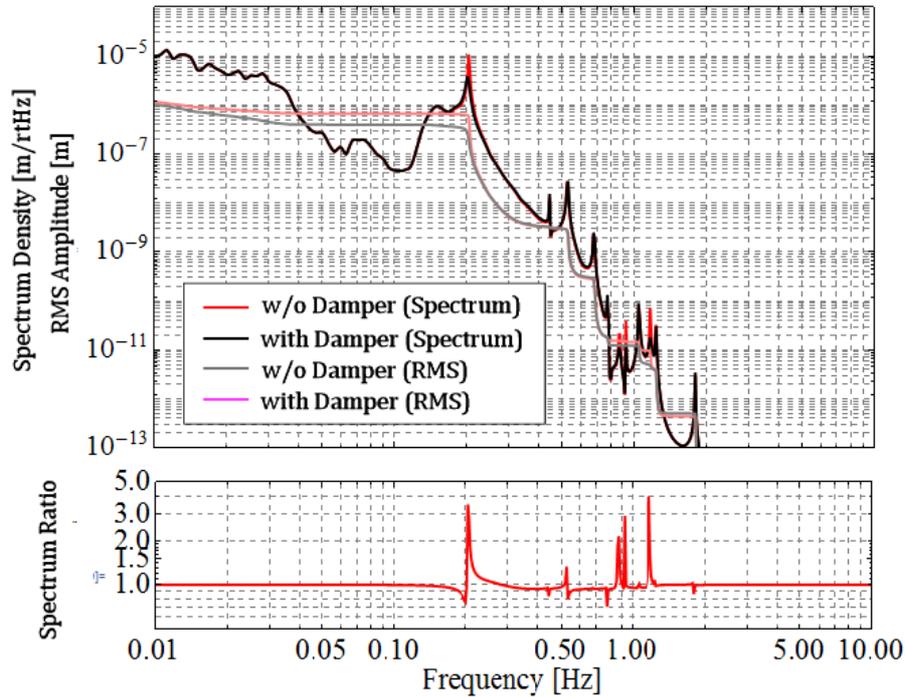
Figure 6.11: The longitudinal displacement of the test mass induced by seismic motion with and without the damper. The lower subplot shows the ratio of the two power spectra.
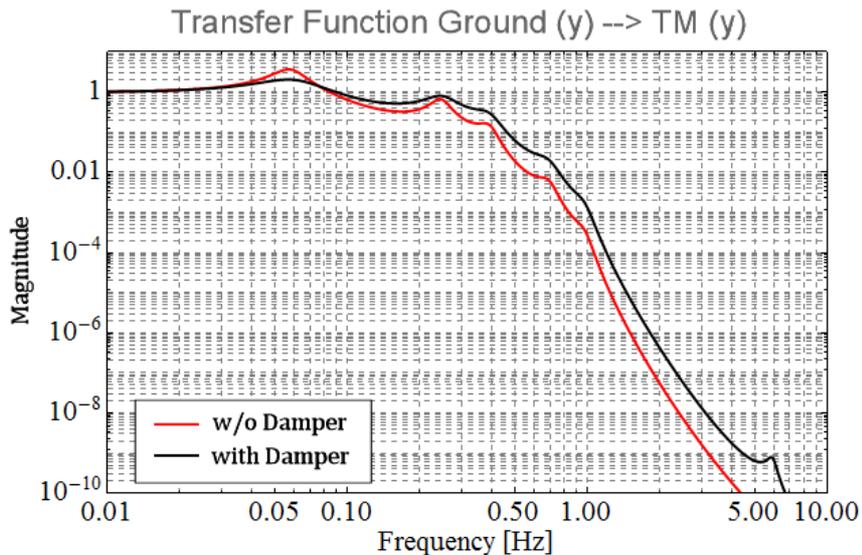

Figure 6.12: Transfer function from the vertical ground displacement to vertical the test mass displacement. The vibration trasmittion through the heat links is not taken into account here.

into account. Thus, the calculated displacement is dominated by the couplings from the vertical noise above ~ 5 Hz. Although the vertical attenuation performance is degraded by the viscous damper around 3-10 Hz, the performance is recovered above the vertical bounce mode frequency of the damper suspension (10 Hz), and the seismic noise of the beam splitter remains at the low level.
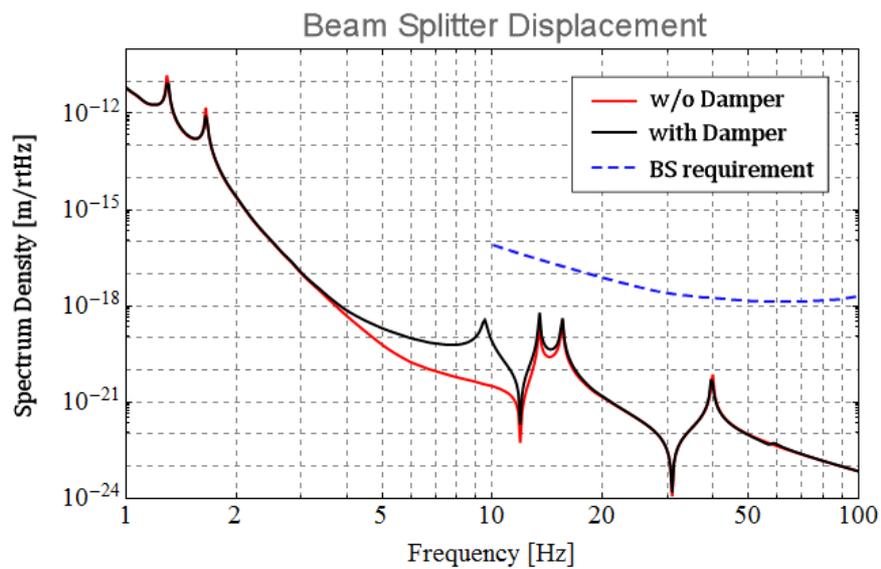
Figure 6.13: The longitudinal displacement of the beam splitter with and without the magnetic damper.

Chapter 7

Summary

In this works, I developed three-dimensional rigid-body models of the vibration isolation systems for LCGT and performed mechanical simulations. The results of the simulations are summarized here.

First, from the given geometry and physical parameters, the attenuation performances of the vibration isolation systems and the residual displacements of the mirrors are estimated. In the type-A system (for the test mass), the seismic vibration transmits to the test mass through two paths: from the top through the attenuation chain and from the cryostat through the heat links. Above 1 Hz, the vibration through the heat links is more significant. It turns out that in the current design, the estimated seismic noise level is barely below the target sensitivity level at the frequency 10-100 Hz and it can possibly pollute the interferometer sensitivity. Therefore two kinds of design arrangement are suggested here: an improved arrangement of the heat link wiring, and the pre-isolation of the cryostat vibration. In both cases, the attenuation performance can be improved by 2-3 orders of magnitude at the frequency of interest (> 10 Hz). The attenuation performance of the type-B system (for the recycling mirrors and the beam splitter) is also estimated, and it turns out that the residual displacements of the mirrors at $> 10 Hz$ are sufficiently lower than the required levels.

Secondly, to estimate the mirror angular displacements, mechanical imperfections (asymmetries) are introduced to the systems. In the calculation, asymmetries are randomly introduced and the computation is iterated for many times (Monte Carlo simulation). The asymmetries introduced to the systems are, the asymmetry in the IP stiffness, the deviation of the suspension point positions, the asymmetry in the wire length and thickness, and the asymmetric wiring of the heat links. The power spectra of the angular displacements are calculated, and then assuming 1 mm mis-centering of the beam spot, the possible couplings to the longitudinal displacement noise are estimated. From the given asymmetries and mis-centering level of the beam spot, the impact on the interferometer sensitivity by the angular fluctuation was found to be much smaller than the impact by the translational motions.

Finally, the passive damping to mitigate the interferometer instablity by the large torsional motions of the mechanical chain is developed. To damp the torsion modes, an eddy current damper is adopted at the top of the chain. The torsional stiffness of the wires are designed so that all the torsion modes of the chain are damped passively at the top. The simulation demonstrates that the damper can successfully damp all the torsion modes

with the decay time of $\sim$ 1 minute. The damper is also capable of damp the pendulum modes and the vertical modes of the attenuation chain, thus the damping effects on the horizontal and vertical attenuation performances are investigated. The simulation shows that the damper can damp several pendulum modes and contribute to the reduction of the mirror RMS displacement. Since the damper is suspended by solid wires from the top stage, the vertical attenuation performance is degraded by the viscous damping force below 10 Hz. Nevertheless, it does not degrade the attenuation performance at the gravitational-wave observation frequency band ($>$ 10 HZ).

Acknowledgement

Bibliography

[1] M. Maggiore. "Gravitational Waves: Theory and Experiments". Oxford University Press, (2008).

[2] T. Nakamura, N. Mio, and M. Ohashi. "Detecting gravitational waves". Kyoto University Press, (1998). (in Japanese).

[3] J. Abadie et al., *Class. Quantum Grav.*, **27**, 173001, (2010).

[4] C. D. Ott, *Class. Quantum Grav.*, **26**, 063001, (2009).

[5] N. Andersson et al., *Gen. Relativ. Gravit.*, **43**, 409–436, (2011).

[6] S. Babak et al., *Class. Quantum Grav.*, **28**, 114001, (2011).

[7] J. Weber, *Phys. Rev. Lett.*, **22**, 1320–1324, (1969).

[8] K. Kawabe, *PhD thesis*, University of Tokyo, (1998).

[9] P. R. Saulson, *Phys. Rev. D*, **42** (8), 2437–2445, (1990).

[10] W. J. Startin et al., *Rev. Sci. Instrum.*, **69** (10), 3681–3689, (1998).

[11] S. Rowan et al., *Phys. Lett. A*, **265**, 40309, (2000).

[12] T. Tomaru et al., *Phys. Lett. A*, **301**, 215–219, (2002).

[13] M. Ando, *PhD thesis*, University of Tokyo, (1998).

[14] H. J. Kimble et al., *Phys. Rev. D*, **65**, 022002, (2001).

[15] J. Hough, *Progr. Part. Nucl. Phys.*, **66**, 233–238, (2011).

[16] K. Arai et al., *Class. Quantum Grav.*, **26**, 204020, (2009).

[17] H. Grote (for the LIGO Scientific Collaboration), *Class. Quantum Grav.*, **27**, 084003, (2010).

[18] D. Sigg (for the LIGO Science Collaboration), *Class. Quantum Grav.*, **25**, 114041, (2008).

[19] T. Accadia et al., *Class. Quantum Grav.*, **28**, 114002, (2011).

[20] K. Kuroda and LCGT collaboration, *Int. J. Mod. Phys. D*, **20** (10), 1755–1770, (2011).

[21] M. Punturo, *Class. Quantum Grav.*, **27**, 194002, (2010).

[22] `http://lisa.nasa.gov/`.

[23] M. Ando et al., *Class. Quantum Grav.*, **27**, 084010, (2010).

[24] Y. Ikushima et al., *Cryogenics*, **48**, 406–412, (2008).

[25] R. Takahashi and Y. Saito, *Vacuum*, **84**, 709–712, (2010).

[26] `http://gwcenter.icrr.u-tokyo.ac.jp/en/researcher/parameter`.

[27] "LCGT Design Document Ver. 3.0". (in Japanese, 2009) available from `http://gwwiki.icrr.u-tokyo.ac.jp/JGWwiki/LCGT`.

[28] M. G. Beker et al., *Gen. Relativ. Gravit.*, **43**, 623–656, (2011).

[29] S. Kedar and F. H. Webb, *Science*, **307**, 682, (2005).

[30] P. Shearer. "Introduction to Seismology Second Edition". Cambridge Univirsity Press, (2009).

[31] H. A. Sodano et al., *J. Vib. Acoust.*, **128**, 294–302, (2006).

[32] T. Nishi, *Master's thesis*, University of Tokyo, (2003). (in Japanese).

[33] Y. Aso et al., *arXiv*, **1111.7147v1 [gr-qc]**, (2011).

[34] A. Takamori, *PhD thesis*, University of Tokyo, (2002).

[35] A. Stochino et al., *Nucl. Instrum. Methods A*, **598**, 737–759, (2009).

[36] A. Bertolini et al., *Nucl. Instrum. Methods A*, **556**, 616–623, (2006).

[37] H. Tariq et al., *Nucl. Instrum. Methods A*, **489**, 570–576, (2002).

[38] C. Wange et al., *Nucl. Instrum. Methods A*, **489**, 563–569, (2002).

[39] K. Agatsuma et al., *Journal of Physics: Conference Series*, **122**, 012013, (2008).

[40] G. Losurdo et al., *Rev. Sci. Instrum.*, **72** (9), 3653–3661, (2001).

[41] F. Cordero et al., *J. Alloys Compd.*, **310**, 400–404, (2000).

[42] M. Beccaria et al., *Nucl. Instrum. Methods A*, **404**, 455–469, (1998).

[43] A. Bernardini et al., *Rev. Sci. Instrum.*, **70** (8), 3463–3472, (1999).

[44] A. Takamori et al., *Class. Quantum Grav.*, **19**, 1615–1621, (2002).

[45] S. Aston, *LIGO Internal Document*, **T050111-04-K**, (2009).

[46] A. Takamori et al., *Nucl. Instrum. Methods A*, **582**, 683–692, (2007).

[47] G. Losurdo et al., *Rev. Sci. Instrum.*, **70** (5), 2507–2515, (1999).

[48] G. Cella et al., *Nucl. Instrum. Methods A*, **540**, 502–519, (2005).

[49] R. DeSalvo et al., *Eur. Phys. J. Plus*, **126**, 75, (2011).

[50] M. Barton et al., *LIGO Internal Document*, **T010007-05**, (2008).

[51] H. Goldstein et al. "Classcal Mechanics Third Edition". Pearson Education International, (2002).

[52] K. Yamamoto, *Master's thesis*, University of Tokyo, (1997). (in Japanese).

[53] K. Somiya, *arXiv*, **1111.7185v1 [gr-qc]**, (2011).

[54] F. Piergiovanni et al., *Virgo Internal Document*, **VIR-015E-09**, (2009).

[55] G. Hammond, *LIGO Internal Document*, **T010171-00-D**, (2001).

[56] G. Cagnoli et al., *Phys. Lett. A*, **272**, 39–45, (2000).

[57] Y. Aso, *LCGT Internal Document*, **JGW-G1000108-v4**, (2010). (presentation file in Japanese), available from `http://gwdoc.icrr.u-tokyo.ac.jp/cgi-bin/DocDB/DocumentDatabase`.

[58] K. Yamamoto et al., *Journal of Physics: Conference Series*, **32**, 418–423, (2006).

[59] Y. Arase et al., *Journal of Physics: Conference Series*, **122**, 012027, (2008).